Title

Integrated analysis of isopentenyl pyrophosphate (IPP) toxicity in isoprenoid-producing Escherichia coli

Authors

George, Kevin W

Thompson, Mitchell G

Kim, Joonhoon

et al.

Publication Date

2018-05-01

DOI

10.1016/j.ymben.2018.03.004

Peer reviewed

Integrated analysis of isopentenyl pyrophosphate (IPP) toxicity in isoprenoid-producing *Escherichia coli*

Kevin W. George[1,2,#], Mitchell Thompson[1,2,3,#], Joonhoon Kim[1,4,#], Edward E. K. Baidoo[1,2], George Wang[1,2], Veronica Teixeira Benites[1,2], Christopher J. Petzold[1,2], Leanne Jade G. Chan[1,2], Suzan Yilmaz[1,2], Petri Turhanen[5], Paul D. Adams[1,6], Jay D. Keasling[1,2,7,8,9], Taek Soon Lee[1,2,*]

[1]Joint BioEnergy Institute, 5885 Hollis Street, Emeryville, CA 94608, USA.

[2]Biological Systems & Engineering Division, Lawrence Berkeley National Laboratory, Berkeley, CA 94720, USA.

[3]Department of Plant and Microbial Biology, University of California, Berkeley, CA 94720, USA

[4]Chemical and Biological Processes Development Group, Pacific Northwest National Laboratory, Richland, WA 99352, USA.

[5]School of Pharmacy, Biocenter Kuopio, University of Eastern Finland, P.O. Box 1627, FIN-70211, Kuopio, Finland

[6]Molecular Biophysics and Integrated Bioimaging Division, Lawrence Berkeley National Laboratory, Berkeley, CA 94720, USA

[7]Department of Bioengineering, University of California, Berkeley, CA 94720, USA

[8]Department of Chemical and Biomolecular Engineering, University of California, Berkeley, CA 94720, USA

[9]The Novo Nordisk Foundation Center for Biosustainability, Technical University of Denmark, Denmark

[#]These authors contributed equally to this work.

*Correspondence: Dr. Taek Soon Lee, Joint BioEnergy Institute, 5885 Hollis St. 4th floor, Emeryville, CA 94608, USA; Phone: +1-510-495-2470, Fax: +1-510-495-2629, E-mail: tslee@lbl.gov

Highlights:

- Three strains at various IPP accumulation levels were comparatively analyzed
- IPP accumulation was linked to decreased cell viability and nutrient uptake
- IPP-induced pathway "breakage" was characterized using multi-omics data
- Nucleotide metabolism and ATP synthesis were perturbed by IPP accumulation
- A nucleotide analog of IPP was identified as a possible contributor to toxicity

Abstract

Isopentenyl pyrophosphate (IPP) toxicity presents a challenge in engineered microbial systems since its formation is unavoidable in terpene biosynthesis. In this work, we develop an experimental platform to study IPP toxicity in isoprenol-producing *Escherichia coli.* We first characterize the physiological response to IPP accumulation, demonstrating that elevated IPP levels are linked to growth inhibition, reduced cell viability, and plasmid instability. We show that IPP toxicity selects for pathway "breakage", using proteomics to identify a reduction in phosphomevalonate kinase (PMK) as a probable recovery mechanism. Next, using multi-omics data, we demonstrate that endogenous *E. coli* metabolism is globally impacted by IPP accumulation, which slows nutrient uptake, decreases ATP levels, and perturbs nucleotide metabolism. We also observe the extracellular accumulation of IPP and present preliminary evidence that IPP can be transported by *E. coli*, findings that might be broadly relevant for the study of isoprenoid biosynthesis. Finally, we discover that IPP accumulation leads to the formation of ApppI, a nucleotide analog of IPP that may contribute to observed toxicity phenotypes. This comprehensive assessment of IPP stress suggests potential strategies for the alleviation of prenyl diphosphate toxicity and highlights possible engineering targets for improved IPP flux and high titer isoprenoid production.

Keywords: Isopentenyl pyrophosphate (IPP), IPP toxicity, isoprenol, ApppI, mevalonate pathway, multi-omics

1. Introduction

The introduction of heterologous metabolic pathways into naive microbial hosts can result in metabolite or product toxicity (Ling et al., 2014). Although natural metabolic pathways have evolved intricate regulation to prevent the buildup of toxic metabolites, heterologous pathways, which frequently consist of non-native reactions from different organisms, typically lack such sophistication (Chubukov et al., 2016). Without regulation, imbalances in assembled pathways frequently lead to metabolite accumulation and toxicity (Jones et al., 2015). Typical metabolic engineering and synthetic biology workflows for improved pathway expression (Boyle and Silver, 2012; Jullesson et al., 2015; Keasling, 2012) may amplify this issue by causing massive fluctuations in metabolite concentrations. Even if a pathway is well-balanced, many chemicals targeted for microbial production are toxic at the concentrations that are necessary for economical, industrial-scale production (Nicolaou et al., 2010). The practical importance of addressing this toxicity has resulted in numerous studies aimed at interrogating and alleviating product toxicity in common industrial hosts such as *Escherichia coli* and *Saccharomyces cerevisiae* (Mukhopadhyay, 2015).

Assessment of product or intermediate toxicity is challenging, particularly in an engineered host that produces the molecules *in vivo.* In engineered microbes harboring heterologous pathways, increased metabolic burden (Wu et al., 2016) and unexpected impacts on endogenous metabolism make the isolated study of metabolite toxicity difficult. To avoid this complexity, most studies have relied on well-controlled systems where the toxic product is exogenously added to the wild-type host and systems analyses are employed to study the stress response (Brynildsen and Liao, 2009). Though multiple studies have successfully used these approaches, there are several limitations. For example, exogenous addition is only successful

when the compound of interest crosses the cell membrane through active transport or diffusion (Mukhopadhyay, 2015). While this is not an issue for solvents such as isobutanol (Atsumi et al., 2010), many toxic intermediates or products contain functional groups that prevent membrane transport. Even if the compound is transported, it is unclear if the stress response associated with exogenous addition reflects the response associated with *in vivo* production. This is particularly true for a wild type host, which likely has different metabolism and overall fitness compared to an extensively engineered production strain (Wu et al., 2016). Finally, exogenous addition can introduce unintended artifacts or impurities to the experimental system. In the case of limonene, for instance, extended chemical storage forms hydroperoxide derivatives that are significantly more toxic than limonene itself (Chubukov et al., 2015).

The *S. cerevisiae* mevalonate pathway for isoprenoid biosynthesis has been heavily engineered to produce valuable compounds including the anti-malarial drug artemisinin (Paddon and Keasling, 2014) and several candidate biofuels (George et al., 2015a). Considerable progress has been made in the production of isoprenol, a C5 alcohol derived from isopentenyl pyrophosphate (IPP), which is one of two universal precursors for isoprenoid compounds (George et al., 2015b; Zheng et al., 2013). In *E. coli*, the toxicity of both isoprenol (Foo et al., 2014) and IPP (George et al., 2014) has been suggested to impact cell growth and limit product yields. Although the toxicity of IPP (and its longer chain derivatives GPP and FPP) was observed over a decade ago (Martin et al., 2003), a systematic assessment of this stress and its impact on host physiology has yet to be conducted. Metabolic engineering strategies have instead focused on avoiding its accumulation, primarily through careful pathway "balancing", improved expression of terminal enzymes, and, most recently, through the assembly of alternative pathways (Kang et al, 2016). Since IPP is a universal precursor for isoprenoid

compounds, understanding its mode of toxicity could benefit engineering in a variety of hosts and pathway variants. More broadly, uncovering the mechanism of IPP toxicity could hold biological relevance for the study of isoprenoid pathway regulation in a variety of organisms.

In this work, we developed a three-strain experimental system to study IPP toxicity *in vivo* in isoprenol-producing *E. coli*. First, we assessed the impact of IPP accumulation on host physiology by measuring growth characteristics, morphology, and viability. Informed by these data, we next collected comprehensive metabolomics and proteomics measurements over an 18-hour fermentation time course. We used principal component analysis (PCA) to direct our investigation, which linked IPP accumulation to reduced nutrient uptake, a "pause" in metabolism, and reduced ATP levels. Finally, we performed RNA-seq at critical time points corresponding to the onset and alleviation of IPP-induced toxicity. We use these complementary data to propose a possible mechanism for IPP toxicity involving the formation of an isoprenyl-ATP analog, ApppI.

2. Material and Methods

2.1. Strains and Culture Conditions

Derivatives of *E. coli* DH1 WT EV (DH1 harboring pBbA5c and pTrc99A), 3A (DH1 harboring pJBEI-6829 and pJBEI-6833), and 3Amk (DH1 harboring pJBEI-6829 and pJBEI-6834) were used in this study. Overnight cultures were grown in 10 mL of LB media supplemented with 30 µM chloramphenicol (Cm_{30}) and 100 µM carbenicillin ($Carb_{100}$). Cultures were inoculated directly from frozen glycerol stocks and incubating overnight at 37°C. Production experiments were carried out in 200 mL of EZ-Rich defined medium (Teknova, Hollister, CA) in 1 L non-baffled Erlenmeyer flasks. EZ-Rich medium was supplemented with

1% w/v glucose as well and Cm_{30} and $Carb_{100}$. Overnight cultures were diluted to an initial OD_{600} of 0.1 and incubated at 37°C shaking at 200 rpm until OD_{600} reached ~0.4-0.6. When the desired OD_{600} was reached, cultures were induced with IPTG to a final concentration of 500 µM and moved to 30°C shaking at 200 rpm. Re-inoculation experiments to examine pathway breakage were conducted by inoculating fresh EZ-Rich medium 1:50 with production culture after 20 hours.

2.2. Evaluation of IPP Toxicity on Physiology

To evaluate the effects of IPP buildup on *E. coli* physiology we measured CFU/mL in production curves at 0, 6, 12, and 24 hours post-induction. Cultures were serially diluted 10-fold and then spread on LB agar plates. Colony counts were made after overnight incubation at 37°C. We also determined cell viability at 0, 1, 3, 6, 9, and 12 hours post-induction by combining nucleic acid staining with flow cytometry. To measure cell viability, cells were stained with nucleic acid-binding dyes SYTO®9 and propidium iodide (PI) at a final concentration of 5 µM and 20 µM, respectively (Thermo Fisher Scientific, Waltham, MA) for 15 min at room temperature according to the manufacturer's instructions. Quantitative measurements of population viability were done via a BD FACS Aria II, equipped with 488-, 561-, and 633-nm solid-state lasers and a forward scatter PMT (BD Biosciences, San Jose, CA). After staining cells were diluted to approximately 10^6 cells/mL in PBS, and a calibrated suspension of 6 µm polystyrene microbeads was added to samples at a density of $1x10^6$ beads/mL to serve as a counting standard prior to the data acquisition on the flow cytometer. A 488-nm (blue) laser was used for SYTO®9 and PI excitation, and fluorescence emission was detected using a 530/30 bandpass filter for SYTO® 9 fluorescence and a 575/25 bandpass filter for PI fluorescence. For

each sample, 10,000 events were collected at a throughput rate of 1000 events/s, using side scatter and forward scatter thresholds of 200. All flow cytometry data were analyzed with the FlowJo package (v X.0.7) (TreeStar Inc., Ashland, OR). Red fluorescence versus green fluorescence scattogram was used to discriminate live and dead populations, and cell concentrations were determined from the ratio of cell events to microsphere events in the scattogram. Stained cells were also visualized on a Leica DMC 4000 microscope using a Hamamatsu ORCA flash-4.0LT camera using a 63× objective.

2.3. Sampling and Sample Storage

To sample non-isoprenol metabolites, 1.8 mL of culture was collected in 2 mL microfuge tubes at times 0, 0.5, 1, 3, 6, 9, 12, 15, and 18 hours post-induction. From this sample 0.1 mL was used to measure OD_{600}, and 0.2 mL was frozen at -20°C to measure isoprenol. The remaining 1.5 mL were pelleted at 14,000 rpm in tabletop centrifuge. Subsequently 0.25 mL of supernatant was frozen at -20°C directly for HPLC analysis of organic acids, and an additional 0.25 mL was mixed 1:1 in ice-cold MeOH and stored at -20°C for LC-MS investigation of extracellular metabolites. The remaining supernatant was decanted and the pellet was resuspended in 0.2 mL of ice-cold MeOH and stored at -20°C to investigate intracellular metabolites. To quantify cellular proteins 5 mL of culture was sampled at the same time points as metabolites and centrifuged at 5000 g for 15 minutes. Samples were then decanted and stored at -80°C. RNA sample were taken at 0, 1, and 12 hours after induction. Volumes corresponding to 1E9 CFU/mL were immediately quenched in 2 volumes of RNAlater (Ambion) and left to stabilize for 5 minutes at room temperature. Samples were then pelleted at 5000 g for 15 minutes, decanted and stored at -80°C.

2.4. Isoprenol Quantification

Isoprenol was quantified by adding 200 µL of ethyl acetate to samples and vortexing microfuge tubes at maximum speed on for 15 minutes using a foam adapter. Samples were then centrifuged at 14,000 rpm for 1 minute. Samples from time points 0, 0.5, 1, 3 had 100 µL of the organic (top) phase moved directly into Agilent glass inserts placed into amber GC Vials. The remaining time points had 100 µL of the organic phase diluted into 400 µL of ethyl acetate in amber GC vials. Standard curves for diluted and undiluted samples were run in concert with samples from the experiment. Isoprenol concentration was measured by GC-FID (George et al., 2015a).

2.5. Metabolomics Processing

Extracellular (supernatant) samples were spun through 3kDa filters (Millipore) at 14,000 rpm for 1 hour at 4°C and then stored at -20°C. Intracellular (cell pellet) samples were mixed with an equal volume of HPLC grade water (200 µL) and vortexed for 10 seconds. Samples were then pelleted at 14,000 g for 4 minutes at 4°C. Subsequently 300 µL of supernatant was spun through a 3kDa filter (Millipore) for 1 hour at 4°C. Approximately 250 µL of samples passed through the filter and were brought up to 1mL in volume with ice-cold HPLC-grade water. Tubes were then covered in parafilm and had three small holes poked into the top. Samples were then flash frozen in liquid nitrogen and placed into metal blocks that had previously been stored at -80°C for 1 hour. Frozen samples were then freeze-dried for 48 hours. Freeze dried pellets were then resuspended in 90 µL of mobile phase and metabolites were separated via a SeQuant® ZIC®-pHILIC guard column (20-mm length, 2.1-mm internal

diameter, and 5-µm particle size; from EMD Millipore, Billerica, MA, USA), in series with a short SeQuant® ZIC®-pHILIC column (50-mm length, 2.1-mm internal diameter, and 5-µm particle size) and a long SeQuant® ZIC®-pHILIC column (150-mm length, 2.1-mm internal diameter, and 5-µm particle size) using an Agilent Technologies 1200 Series Rapid Resolution HPLC system (Agilent Technologies, Santa Clara, CA, USA). Thus, the mobile phase flow path was from guard column → short column → long column → time-of-flight mass spectrometer (TOF-MS). Sample injection volume, autosampler tray temperature and column compartment were set to 2 µL, 6°C, and 40°C, respectively. The mobile phase was composed of 10 mM ammonium carbonate (Fluka Analytical, Sigma-Aldrich, St. Louis, MO, USA) and 118.4 mM ammonium hydroxide (from a 14.8 M ammonium hydroxide solution, EMD Chemicals, Billerica, MA, USA) in acetonitrile-water (60.2:39.8, v/v). Metabolites were eluted isocratically via a flow rate of 0.18 mL/min from 0 to 5.4 min, which was increased to 0.27 mL/min from 5.4 to 5.7 min, and held at this flow rate for an additional 5.4 min, giving a total run time of 11.1 min. The HPLC system was coupled to an Agilent Technologies 6210 TOF-MS system. Electrospray ionization (ESI) was conducted in the negative ion mode for the detection of $[M - H]^-$ ions. Data acquisition and processing were performed by the Agilent MassHunter software package. Visualization and principal component analysis were performed in a Jupyter R notebook, "IPP_metabolomics" (**Supplemental File S1**).

2.6. Proteomic Processing and Analysis

Protein lysis and precipitation were achieved by using a chloroform-methanol extraction as previously described. Thawed pellets were loosened from 14 mL falcon tubes and transferred to 1.5 mL tubes, followed by the addition of 400 µL of methanol, 100 µL of chloroform, and 300

µL of water, with vortexing in between each addition. The samples were centrifuged at 21,000 x g for 1 minute for phase separation. The methanol and water top layer was removed, then 300 µL of methanol was added and the sample was vortexed. The samples were centrifuged at 21,000 x g for 2 minutes to isolate the protein pellet. The protein pellet was dried for 5 minutes at 30ºC in a vacuum concentrator and resuspended in 100 mM ammonium bicarbonate with 20% methanol. The protein concentration was measured using the DC Protein Assay Kit (Bio-Rad, Hercules, CA) with bovine serum albumin for the standard curve. A total of 200 µg of protein from each sample was digested with trypsin for shotgun proteomic analysis. The protein was reduced by adding tris 2-(carboxyethyl) phosphine (TCEP) at a final concentration of 5 mM and incubating at room temperature for 30 minutes. The protein was then alkylated by adding iodoacetamide at a final concentration of 10 mM and incubating for 30 minutes in the dark. Trypsin was added at a ratio of 1:50 trypsin:total protein and the samples were incubated overnight at 37ºC.

As previously described (González Fernández-Niño et al., 2015), peptides were analyzed using an Agilent 1290 liquid chromatography system coupled to an Agilent 6550 QTOF mass spectrometer (Agilent Technologies, Santa Clara, CA). Peptide samples (20 µg) were separated on an Ascentis Express Peptide ES-C18 column (2.7 µm particle size, 160 Å pore size, 10 cm length x 2.1 mm i.d., 60 ºC; Sigma-Aldrich, St. Louis, MO) by using a chromatographic gradient (400 µL/min flow rate) with an initial condition of 95% Buffer A (99.9% water, 0.1% formic acid) and 5% Buffer B (99.9% acetonitrile, 0.1% formic acid) then increasing linearly to 65% Buffer A/35% Buffer B over 30 minutes. Buffer B was then increased to 80% over 1 minute and the held at 80% for 5 minutes followed by ramping back down in 1 minute to 5% Buffer B where it was held for 7 minutes to re-equilibrate the column for the next sample.

Data were converted to '.mgf' files for analysis with Mascot version 2.3.02 (Matrix Science, Boston, MA) with the following parameters: peptide tolerance of ±50 ppm and MS/MS tolerance of ±0.1Da; fixed modifications Carbamidomethyl (C); variable modifications Oxidation (M); up to one missed cleavage for trypsin; peptide charge 2+, 3+, and 4+. Searches were performed against an *E. coli* (strain K12) dataset obtained from UniProt with additional proteins associated with the engineered pathway and common contaminant proteins appended to it. The protein and peptide matches from Mascot were refined by using Scaffold version 4.3 (Proteome Software Inc.).

2.7. Transcriptomic (RNAseq) Processing and Analysis

Total RNA was isolated using the Qiagen RNeasy minikit (Qiagen) according to Protocol 2. Manufacturer's instructions were followed exactly. RNA was eluted in one step in 45 µL of RNase free water. Total RNA was then treated with TURBO DNase (Ambion) according to manufacturer's instructions. DNase was then removed with the DNase inactivation reagent and removed from the sample at -80°C. RNAseq was performed by the Vincent J. Coates Genomics Sequencing Laboratory at the California Institute for Quantitative Biosciences where rRNA was depleted and sequencing was performed on an Illumina 50SR HiSeq 2000 sequencer. FASTQ files were then trimmed and quality filtered using BBDuk, reads were mapped to a DH1 reference genome via bwa-mem (Li and Durbin, 2009), transcript counts were then quantified via featureCounts (Liao et al., 2014), and then differential expression was calculated via DESeq2 (Love et al., 2014). The RNAseq data have been deposited in NCBI's Gene Expression Omnibus and are accessible through GEO Series accession number GSE102672 (https://www.ncbi.nlm.nih.gov/geo/query/acc.cgi?acc=GSE102672). Functional enrichment

analysis using clusterProfiler (Yu et al., 2012) and visualization using Cytoscape via RCy3 (Shannon et al., 2013) were performed in a Jupyter R notebook, "IPP_transcriptomics" (**Supplemental File S2**).

2.8. Synthesis of ApppI

Standard sample of ApppI was prepared by Dr. Petri Turhanen's research team according to the procedure described in the reference (Weisell et al., 2015).

3. Results

3.1. Developing a platform to selectively assess *in vivo* IPP toxicity

The heterologous pathway for isoprenol production in *E. coli* consists of 8 reactions, 7 of which are catalyzed by plasmid-borne genes (**Figure 1A**). It was previously demonstrated through proteomics analysis that the level of mevalonate kinase (MK) is the primary determinant of downstream pathway flux to IPP (George et al., 2014). We took advantage of this relationship to develop an experimental platform to isolate the impact of IPP toxicity from heterologous pathway induction (e.g., metabolic burden) and isoprenol production. This platform consisted of three strains (**Figure 1B**): (1) strain 3A, a balanced, high-yield isoprenol production strain of *E. coli* DH1 harboring two isoprenol pathway plasmids; (2) strain 3Amk, a modified version of strain 3A that expresses ~10-fold more MK protein and accumulates IPP; and (3) DH1-EV ("empty vectors", also referred to as WT), *E. coli* DH1 carrying promoter-less plasmid backbones with the same origin and antibiotic markers as those in 3A and 3Amk.

We first measured optical cell density (OD), intracellular IPP concentration, and extracellular isoprenol levels in each strain to ensure the experimental system was functioning as

expected (**Figure 1C**). Significant growth inhibition was observed in strain 3Amk relative to strain 3A following induction, correlating with elevated IPP levels (~370 mM peak concentration in strain 3Amk vs. 40 mM in strain 3A). The growth of an uninduced 3Amk control was not inhibited (**Supplemental Figure S1**). IPP levels in strain 3Amk peaked at 3 hours post-induction and subsequently decreased for the remainder of the time course. The growth rate decreased substantially 3 hours post-induction when IPP levels were at their highest, suggesting an inverse correlation between IPP levels and growth rate. By 18 hours, the OD of strain 3Amk matched that of strain 3A, although the growth rates observed from 8 to 18 hours were reduced relative to strain 3A. Isoprenol titer was low in strain 3Amk compared to strain 3A: by 18 hours, strain 3Amk produced 180 mg/L of isoprenol compared to the ~600 mg/L produced by strain 3A. The growth rate of strain 3A was nearly the same as that of the WT despite the accumulation of IPP to a concentration of ~40 mM, setting an approximate range of IPP toxicity between ~40 mM and ~250 mM (the IPP concentration in strain 3Amk when growth defects became apparent).

3.2. IPP accumulation leads to morphological defects, decreased viability, and reduced plasmid stability

We next examined the physiology of each strain to assess the impact of IPP accumulation. To do so, we compared the morphology and viability of strain 3A and 3Amk using microscopy, live/dead staining, and CFU counts (**Figure 2**). Following pathway induction, we observed an increase in dead or metabolically inactive cells in strain 3Amk (**Figure 2A**). Strain 3A remained viable through the time course, with <1% of cells characterized as dead, compared to >10% in strain 3Amk. Microscopy of live/dead stained cells from strain

3Amk (**Figure 2B**) and strain 3A (**Figure 2C**) showed clear morphological differences. We observed elongated cells in strain 3Amk and a staining phenotype consistent with compromised membrane integrity. We next measured CFUs on solid media to determine if IPP accumulation affected the strains' ability to form viable colonies (**Figure 2D**). Surprisingly, CFU counts decreased in strain 3Amk from 0 (pre-induction) to 6 hours. This decrease in CFUs occurred despite a ~3-fold increase in OD during the same period. By 24 hours, CFU counts in strain 3Amk recovered, matching strain 3A. To determine if strain 3Amk's recovery was the result of plasmid loss, we compared CFUs recovered on selective media (i.e., LB chloramphenicol to select for plasmid 1 and LB carbenicillin for plasmid 2) to those recovered on non-selective media. For strain 3Amk, CFU counts on selective media were ~40% lower than those on non-selective media at 24 hours, suggestive of partial plasmid loss (**Figure 2E**). No such loss was observed for strain 3A, where CFUs recovered on selective and non-selective media were identical (**Figure 2F**). Loss of plasmid 1 was first apparent at 6 hours post-induction, while plasmid 2 instability was not observed until 12 hours post-induction. Intriguingly, all populations recovered as IPP levels decreased (i.e., from 6 to 24 hours), implying that plasmid loss is not responsible for growth recovery. Still, the fact that plasmid loss occurred only in strain 3Amk suggests that IPP production is detrimental to strain stability, a factor that is particularly important for fed-batch fermentation and scale-up.

Physiological observations indicated that IPP accumulation was associated with significant changes in growth rate, cell morphology, cell viability, and plasmid stability. Importantly, *E. coli* appeared to recover from these perturbations as IPP concentrations decreased. To explore the nature of this recovery, we next collected metabolomics and proteomics data to identify potential changes in pathway function.

3.3. IPP accumulation is associated with MVA pathway "breakage"

The production of a toxic intermediate can lead to heterologous pathway "breakage" through regulatory feedback or the selection of mutations that attenuate pathway flux and thus reduce toxicity (Jones et al., 2015). In strain 3Amk, the rapid decrease in peak IPP levels and associated growth recovery suggested that breakage might have occurred, although the continued production of isoprenol implied that the heterologous pathway was at least partially functional. To investigate, we measured pathway metabolites and proteins in strains 3A and 3Amk over an 18-hour time course.

Pathway proteins were stable except for phosphomevalonate kinase (PMK), which unexpectedly decreased in concentration by 8-fold in strain 3Amk from 6 hours to 18 hours post-induction (**Figure 3A**). No such decrease was observed in strain 3A. Though minor plasmid loss occurs in strain 3Amk (**Figure 2E**), the selective decrease of PMK protein (rather than a decline in all pathway proteins) suggested an alternative cause. Decreased PMK appeared to affect pathway flux as levels of Mev-PP, the product of the PMK reaction, declined abruptly beginning at 6 hours post-induction (**Figure 3B**). IPP levels also fell, though this decrease began at 3 hours suggesting multiple mechanisms might be responsible for IPP reduction. Note that HMG-CoA, which was previously shown to be toxic (Kizer et al., 2008), was produced at similar levels in both strains (< 1 mM). Although PMK was the only protein that dynamically declined, the absolute levels of PMD and NudB were ~40% lower in strain 3Amk than strain 3A. Partial plasmid loss could contribute to decreased PMD and NudB, though if this was the sole cause then similar responses would be expected for all pathway proteins since both plasmids are unstable in strain 3Amk. Decreased levels of LacI and β-Lactamase (**Supplemental Figure S2**),

proteins that were encoded on the same plasmid as NudB and PMD (plasmid 2, **Figure 1B**), were also observed, suggesting that plasmid 2 might be maintained at a lower copy in strain 3Amk. Regardless of the explanation, NudB and PMD remained the most abundant pathway proteins in strain 3Amk and are unlikely to act as bottlenecks at this concentration (George et al., 2014). Consequently, we focused on PMK since its decrease had an obvious impact on pathway function.

Intriguingly, degradation or even complete loss of PMK will still permit isoprenol production due to the existence of the "IPP bypass" pathway: the promiscuous activity of PMD results in decarboxylation of Mev-P into IP, which is converted into isoprenol through the activity of multiple *E. coli* native phosphatases (Kang et al., 2016). This "IPP bypass" (**Figure 3C**) avoids the complications of IPP formation, provides an outlet for Mev-P (which might otherwise be expected to accumulate), and permits the continued production of isoprenol in strain 3Amk (**Figure 3C**). More importantly, implementation of this alternative pathway may contribute to strain 3Amk's recovery later in the time course.

We suspected that the minor plasmid loss, reduced viability, and pathway "breakage" associated with IPP accumulation would lead to significant strain instability over multiple generations. To investigate, we collected biomass from strain 3A and 3Amk following a 24-hour production time course ("primary" cultures) and inoculated fresh cultures ("secondary" cultures) that were monitored for growth, intracellular IPP levels, and isoprenol production. Antibiotic selection was maintained in both cultures to ensure that any observed phenotypes were not solely due to plasmid loss. We hypothesized that pathway "breakage" and growth selection would result in a secondary 3Amk culture with reduced IPP accumulation and rapid growth. As anticipated, the growth rate of the secondary 3Amk culture was dramatically increased,

exceeding even the primary culture of strain 3A (**Supplemental Figure S3**). While the primary culture predictably accumulated IPP at high concentrations, IPP was at wild-type levels in the secondary culture. Intriguingly, isoprenol was below detection in the secondary 3Amk culture, suggesting that PMK is perhaps only one of multiple pathway nodes that are susceptible to breakage over time. There was also evidence of minor pathway breakage in the secondary 3A culture, though the continued production of isoprenol showed the pathway was marginally functional. These results underscore the deleterious effect of IPP accumulation on strain stability and highlight the need for a more comprehensive assessment of the cell's metabolic response to IPP exposure.

3.4. IPP accumulation is correlated with reduced nutrient uptake, a reduction in ATP levels, and a global "pause" in metabolism

We investigated the impact of IPP accumulation on *E. coli* metabolism by quantifying endogenous metabolites (along with MVA pathway intermediates) in the intracellular (**Figure 4A**) and extracellular matrix (**Figure 4B**). To reduce the complexity of these data, we used principal components analysis (PCA) to identify key drivers of variation between each strain (Brunk et al., 2016). We performed PCA on metabolites found in both the intracellular (**Figure 4C**) and extracellular matrix (**Figure 4D)**, respectively. Please see **Supplemental File S1** (Jupyter R notebook "IPP_metabolomics") for additional detail and analysis.

PCA separated strains 3A, 3Amk, and WT into distinct regions based on the intracellular data set, particularly in a plot of the first 2 principal components (**Figure 4C**). Separation between strains was greatest along PC2 (the vertical axis), where pathway metabolites were the primary contributors to variation. IPP explained more of the variance than any other pathway

metabolite, a strong validation of the experimental system. Separation along PC1 correlated with time of measurement (i.e., early time points towards the left of the x-axis, later time points to the right), with non-pathway metabolites, particularly amino acids, contributing strongly to variation in PC1. Although intracellular levels of most amino acids decreased over time, rates of consumption were significantly decreased in strain 3Amk (**Figure 4A**). Metabolites associated with response to osmotic stress, including proline and glycine betaine, were elevated in strain 3Amk (**Supplemental Figure S4**). Surprisingly, 2-C-methyl-D-erythritol 2,4-cyclodiphosphate (MEcPP), a metabolite in the endogenous 2-C-methyl-D-erythritol 4-phosphate (MEP) pathway for isoprenoid biosynthesis, was a significant driver of variation between strain 3A and strain 3Amk. In strain 3A, MEcPP accumulated to levels exceeding every other MVA pathway intermediate apart from mevalonate by 18 hours. Other MEP pathway intermediates were also detected at elevated levels in strain 3A including MEP and CDP-ME, although these concentrations were more than an order of magnitude lower than MEcPP. Though not identified by PCA, the difference in ATP levels between strain 3A and 3Amk was notable (**Figure 4E**). ATP levels in strain 3Amk fell from 5.2 mM pre-induction to 0.8 mM at 3 hours post-induction. Adenylate energy charge in strain 3Amk was also reduced relative to 3A and DH1, particularly at 1 hour post-induction (**Figure 4E**).

Quantifiable amounts of MVA pathway intermediates were detected in the growth medium of strains 3A and 3Amk. While the presence of mevalonate was expected, we were surprised at the detection of μM concentrations of mono- and diphosphorylated pathway intermediates. For example, IPP accumulated to ~40 μM at 12 hours post-induction in strain 3Amk before declining to less than 10 μM by 18 hours. While this phenomenon was most obvious in strain 3Amk, some phosphorylated intermediates such as IP were detected outside the

cell in both strains. Unsurprisingly, PCA of the extracellular data set (**Figure 4D**) highlighted these pathway metabolites as significant drivers of variation. The strains once again separated primarily along PC2, where isoprenol, extracellular pathway intermediates, and acetate were key drivers of variation. MEcPP was also identified as a significant driver of variation: in strain 3A, extracellular MEcPP concentrations increased over time, suggesting that this molecule was actively exported (**Supplemental Figure S5**). Amino acids explained most of the variation in PC1, which tracked with time of measurement. Amino acid uptake rates were reduced in strain 3Amk relative to strain 3A, particularly during periods of IPP accumulation (i.e., 1 to 9 hours) (**Figure 4B, Figure 4F**). The impact on glucose uptake by 3Amk was even more striking: glucose uptake ceased from 1 to 6 hours post-induction, a timeframe characterized by the highest recorded intracellular concentrations of IPP (**Figure 4F**). Glucose consumption resumed at a rate similar to strain 3A beginning at 12 hours post-induction.

The reversible reduction in cell growth, viability, and nutrient (e.g., glucose and amino acid) uptake suggests that IPP accumulation leads to a "pause" in typical *E. coli* metabolism. Low ATP availability could partially explain this behavior, though it is difficult to determine causation since reduced glucose uptake (and subsequently, reduced glycolytic flux) will itself decrease ATP levels. This is clearly seen in the falling ATP levels of DH1 WT from 10 to 18 hours post-induction (**Figure 4E**), where glucose uptake rates were reduced (**Figure 4F**).

3.5. Evidence of IPP uptake in strain 3Amk

Before continuing our primary analysis, we sought to investigate the unexpected presence of extracellular IPP in strain 3Amk. While cell lysis or membrane leakage could explain its release from the cell, we were intrigued by the declining extracellular concentrations after 12

hours (**Figure 5A**). Specifically, we questioned whether this decline was the result of abiotic degradation, enzymatic transformation, or cellular transport. To clarify this behavior, we designed an experiment to evaluate IPP stability in the production media (**Figure 5B**). A culture of 3Amk was grown to an OD of 0.6, induced with IPTG, and incubated at 30°C using conditions identical to the previous metabolomics time course experiment. At 6 hours post-induction (a period of increasing extracellular IPP) and 15 hours post-induction (a period of decreasing extracellular IPP), supernatant was collected from two 10 mL samples of culture and treated with a 0.2 µm filter (filter-sterilized, or "FS" in **Figure 5**) or a 3kDa molecular weight cut-off filter ("MWCO" in **Figure 5**) to remove residual cells or cells and proteins, respectively. Treated supernatant was incubated with shaking at 30°C and sampled to measure IPP concentrations over time. Supernatant derived from the parent culture ("culture" in **Figure 5**) was also sampled to ensure that the previously observed IPP dynamics were reproducible.

In the supernatant derived from whole cell culture, the previously observed behavior was reproduced (i.e., increasing IPP levels up to 12 hours post-induction, decreasing IPP levels from 12 to 24 hours post-induction). In both the FS and MWCO treatments, however, levels of IPP were unchanged from the time of initial sampling (6 and 15 hours post-induction, **Figure 5C** and **Figure 5D**, respectively) until the end of the time course. These results show that IPP is stable in the culture media and suggest that cellular uptake is the most likely explanation for declining concentrations. Extracellular IP, which shared a similar profile to IPP and was identified in both strains, was also stable in the culture media (**Supplemental Figure S6**) along with all other MVA pathway intermediates. These data suggest that abiotic degradation plays a minimal role in observed metabolite dynamics and offer preliminary evidence that *E. coli* may be capable of transporting phosphorylated MVA pathway intermediates.

3.6. IPP accumulation perturbs nucleotide metabolism and induces genes involved in RNA processing and modification

To further characterize the metabolic "pause" and subsequent recovery, we used RNAseq to identify differentially expressed genes between engineered strains and the wild-type control at time points corresponding with IPP accumulation and reduction in strain 3Amk. We sampled each strain prior to pathway induction (t = 0 hour), at the onset of IPP toxicity in strain 3Amk (t = 1 hour), and during growth recovery in strain 3Amk (t = 12 hours). By comparing the transcriptome of all 3 strains, we hoped to isolate the impact of IPP accumulation (differentially expressed genes in strain 3Amk only) from the impact of heterologous protein expression and metabolic burden (differentially expressed genes in both 3A and 3Amk relative to WT). At 1 hour post-induction, 116 genes were commonly upregulated in strains 3A and 3Amk relative to the empty vector control, while 142 genes were commonly downregulated (**Figure 6A**). There were 140 and 268 genes upregulated in strains 3A only and 3Amk only, respectively, while 176 and 225 were downregulated. At 12 hours post-induction, a similar pattern was observed with a larger number of differentially expressed genes. Please see **Supplemental File S2** (Jupyter R notebook "IPP_transcriptomics") for additional detail and analysis.

We anticipated that functional enrichment of the 493 differentially expressed genes in strain 3Amk at t = 1 hour would provide insight into the cell's initial response to IPP accumulation. Specifically, the onset of the metabolic "pause", which was characterized by reduced glucose uptake and declining ATP levels. Enrichment analysis showed that numerous genes involved in RNA processing and modification were upregulated at 1 hour (**Figure 6B**). Methionine and pyrimidine ribonucleotide biosynthesis were also upregulated, along with genes

involved in tRNA wobble base modification, tRNA processing, and ribosome biogenesis. DNA replication and repair were also uniquely upregulated in strain 3Amk, while the *lexA* repressor of genes involved in SOS response to DNA damage was downregulated (DH1's genotype is *recA1*). These data suggest that IPP accumulation has a significant impact on nucleotide metabolism and DNA and RNA metabolic processes. Intriguingly, genes involved in lipopolysaccharide (LPS) biosynthesis, specifically those that catalyze glycosyl transfer from nucleotide sugars, were significantly downregulated at 1 hour post-induction.

The 12-hour time point was during growth recovery and declining IPP levels in strain 3Amk. During strain 3Amk's recovery, 679 genes spanning multiple functional categories were differentially expressed. The components of the F_1 and F_0 subcomplexes of ATP synthase were strongly upregulated in strain 3Amk at t = 12 hours. Genes associated with purine nucleotide biosynthesis from 5-phospho-α-D-ribose 1-diphosphate were also identified, along with genes related to purine nucleoside monophosphate formation. Also upregulated were genes involved in peptidoglycan metabolism and lipopolysaccharide core region biosynthesis, which was previously downregulated at t = 1 hour. These data suggest that ATP synthesis and cell wall biosynthesis play a significant role in the growth recovery from IPP toxicity in strain 3Amk.

Though we were primarily interested in the transcriptomic response to IPP stress, we also investigated common transcriptomic responses in strain 3A and 3Amk. These genes might be involved in cell's response to the metabolic burden of heterologous pathway expression. At t = 1 hour, genes associated with the response to heat and protein folding were upregulated in both 3A and 3Amk (**Figure 6B**). These include the DnaK chaperone system, and chaperones involved in re-solubilization of aggregated proteins or folding of newly synthesized proteins. It is likely this response is linked to the production of heterologous pathway proteins, which can occupy a

significant portion of the total proteome and comprised 35-40% of total transcript reads in strains 3A and 3Amk. Ribonucleoside-diphosphate reductase and its flavodoxin, responsible for converting ribonucleoside diphosphates to deoxyribonucleoside diphosphates (e.g., ADP to dADP), were also upregulated in both strains. Unexpectedly, genes involved in many common stress responses were downregulated relative to DH1 WT in both 3A and 3Amk. Phosphate starvation response genes were downregulated, potentially in response to the liberation of phosphate groups from IPP during isoprenol production. In addition, tryptophan transport and biosynthesis from 5-phospho-α-D-ribose 1-diphosphate were significantly downregulated in both strains. At t = 12 hours, the overlap between strain 3A and 3Amk increased, perhaps indicative of strain 3Amk's active recovery from IPP toxicity. We observed functional enrichment of genes involved in aerobic respiration, proton and cation transport, and TCA cycle metabolism, all of which were upregulated relative to DH1 WT. DNA recombination was also upregulated. Protein metabolism was broadly downregulated, along with cellular responses to heat and nutrient levels. The numerous shared responses between strain 3A and 3Amk further underscore the broad metabolic impacts of heterologous pathway expression and highlight the utility of our experimental platform: assessment of IPP stress through a direct comparison of strain 3Amk and DH1 WT would yield multiple false-positives.

3.7. IPP accumulation is linked to the formation of a toxic isoprenyl-ATP analog

Our omics data suggested that IPP accumulation results in a metabolic "pause", a significant reduction in the ATP pool, and dramatic changes in the expression of genes involved in nucleotide metabolism. Previous work in eukaryotic cells demonstrated that IPP accumulation due to the inhibition of higher terpene synthesis results in the formation of the toxic isoprenyl-

ATP analog ApppI, which is associated with apoptosis (Mönkkönen et al., 2006) (**Figure 7A**). ApppI is synthesized from AMP and IPP by aminoacyl tRNA synthetases and inhibits the activity of adenosine nucleotide transporter (ANT) (Mönkkönen et al., 2006). Though there is no ANT homolog in *E. coli*, the formation of ATP analogs is associated with toxicity in a variety of organisms (Hong and Pedersen, 2008), and we hypothesized that their formation could contribute to IPP toxicity in *E. coli*.

To examine the feasibility of this hypothesis we searched our LC-MS metabolomics data for a mass corresponding to ApppI (m/z 574). Interestingly, not only was a mass of m/z 574 identified, but the relative abundance of the mass closely mirrored the concentration of IPP in strain 3Amk (**Figure 7B**). Furthermore, the relative abundance was inversely correlated to the intracellular concentration of ATP. Though no standard for ApppI is commercially available, a standard was synthesized as described previously (Weisell et al., 2015). To positively identify the presence of ApppI, we repeated our production fermentations with all three strains and took samples for intracellular metabolites at 3 hours post-induction where we had previously identified the highest concentrations of IPP (**Figure 1C)**. LC-MS analysis positively identified the mass we had previously observed as ApppI by retention time and mass spectra **(Figure 7C**). As in the previous time course, the ApppI peak area was ~10-fold greater in strain 3Amk than strain 3A. No ApppI was detected in the DH1 EV control.

4. Discussion

In this work, we show that IPP toxicity is a complex stress with severe physiological consequences. Elevated levels of IPP caused growth inhibition, reduced cell viability as measured by live/dead staining and CFU counts, and plasmid instability. Several results

suggested that membrane function or integrity were compromised in the presence of IPP, including the observation of cell elongation, increased levels of osmoprotectants such as proline and betaine, and differential expression of genes involved in peptidoglycan and lipopolysaccharide biosynthesis. The unexpected presence of phosphorylated intermediates in extracellular samples of strain 3Amk might also suggest abnormal membrane function. IPP accumulation had an obvious impact on nutrient uptake: IPP was anti-correlated with amino acid consumption, and glucose uptake was completely shut down when IPP levels were their highest. Elevated IPP was also anti-correlated with ATP levels, which declined sharply during the onset of IPP accumulation and remained low until IPP levels were reduced. Transcriptomics showed that the onset of IPP accumulation was associated with significant perturbations in nucleotide metabolism and the induction of DNA repair mechanisms, while recovery from IPP toxicity correlated with increases in ATP and cell wall biosynthesis. Finally, it was shown that IPP accumulation led to the formation of ApppI, a nucleotide analog of IPP that is likely to contribute to IPP toxicity.

The heterologous MVA pathway "broke" in response to IPP accumulation, underscoring the strong selective pressure imposed by IPP toxicity. In our experimental system, the immediate response to IPP accumulation was a reduction of PMK protein levels that led to reduced pathway flux to IPP and implementation of an "IPP bypass". The exact mechanism behind this reduction in PMK is still unclear. No obvious mutations were identified in the *PMK* open reading frame or ribosomal binding site (data not shown). Suggestively, mean transcript levels of *PMK* in strain 3Amk decreased by 60% from t = 1 hour to t = 12 hours, compared to an *increase* of ~100% in strain 3A (**Supplemental Figure S7**). Still, transcript levels of multiple pathway genes decreased from 1 to 12 hours in both strains, and only PMK protein levels in

strain 3Amk declined. These results seem to imply that PMK protein is particularly unstable, or perhaps targeted for degradation. A re-inoculation experiment further highlighted strain instability. The "secondary" culture of strain 3Amk showed no growth inhibition and produced no detectable IPP or isoprenol, indicating that the heterologous pathway was no longer functional. Additional work is needed to fully characterize these breakage mechanisms and engineer mitigations where appropriate. These data suggest that IPP toxicity imposes a fundamental limit to isoprenoid pathway productivity and genetic stability. Until mitigations are implemented, strategies to keep IPP levels low (Chou and Keasling, 2013) or bypass IPP completely (Kang et al., 2016) are particularly valuable.

The presence of IPP in extracellular samples of strain 3Amk was unexpected. We initially hypothesized that the presence of extracellular IPP was an indication of cell lysis, as a phosphorylated intermediate should not passively cross the cell membrane. However, we did not detect other metabolites that should be strictly intracellular (e.g., nucleotides, acetyl-CoA, etc.) in the extracellular media as might be expected with considerable cell lysis. While cell lysis could still play a role in the "export" of IPP, follow-up analysis indicated that IPP is transported, or at least taken-up, by the engineered *E. coli* DH1 used in this study (**Figure 5**). Recent work in mammalian dendritic cells showed that ATP-binding cassette transporter A1 (ABCA1) plays a role in extracellular IPP release (Castella et al., 2017). Several ABC transporters with homology to ABCA1 such as MetN were upregulated in strain 3Amk, though we are unable to link any of these transporters with IPP efflux with the current data set (**Supplemental File S2**, Jupyter R notebook "IPP_transcriptomics"). If confirmed, the presence of as-yet uncharacterized IPP transporters in *E. coli* could be relevant to the study of isoprenoid biosynthesis in plants, which contain a plastid-localized MEP pathway and a cytosolic MVA pathway for isoprenoid

biosynthesis. Researchers studying "cross-talk" between these two pathways have identified IPP as a likely candidate for exchange between the plastid and cytosol, however no plastid-membrane components capable of prenyl diphosphate transport have been identified (Lipko and Swiezewska, 2016). IP has also been highlighted as a potential "exchangeable" intermediate between the plastid and cytosol (Sun et al., 2016), and here, too, we see evidence of transport in *E. coli*. Extracellular IP was detected in strain 3Amk and the comparably "healthy" strain 3A, where IP levels approached 100 µM (**Figure 4B, Supplemental Figure S6**). Numerous transporter families were upregulated in strain 3A or 3Amk, though it is again unclear what impact these transporters might have on IP or IPP transport. Still, these data suggest that prenyl mono- and diphosphate transport might be more common than previously believed. Further investigation into the nature of this transport could yield targets for metabolic engineering and aid efforts to identify IPP/IP transporters in plants and other hosts.

MVA pathway metabolites were not the only phosphorylated intermediates detected in the extracellular media. In strain 3A, the MEP pathway intermediate MEcPP accumulated to ~12 µM in the growth media, while intracellular levels approached 40 mM, a concentration that eclipsed every MVA pathway intermediate except for mevalonate. Extracellular MEcPP was previously observed in *E. coli* with an engineered MEP pathway, where metabolite profiling identified MEcPP efflux as a limiting step in MEP-based isoprenoid production (Zhou et al., 2012). Overexpression of IspG, the enzyme downstream of MEcPP, led to increased lycopene production and reduced concentrations of extracellular MEcPP. The fosmidomycin efflux pump Fsr was suggested to play a potential role in MEcPP export. Though we cannot rule out other transporters, *fsr* was indeed upregulated in strain 3A by ~3.5 fold at 1 hour and ~15.5 fold at 12 hours. Engineering to reduce unwanted MEcPP production (e.g., IspG overexpression) could be

beneficial for isoprenol production or perhaps isoprenoid production in general, although further work is needed to determine the prevalence of this phenomenon in isoprenoid-producing *E. coli*. More broadly, the identification of elevated levels of MEcPP in a strain without MEP pathway engineering hints at potential interplay between the MVA and MEP pathways that warrants further exploration.

The identification of the IPP-nucleotide analog ApppI in this study is, to our knowledge, the first evidence of its formation in prokaryotic systems. In eukaryotes, ApppI is believed to result from a back reaction between IPP and AMP-amino acids catalyzed by aminoacyl tRNA synthetases (Mönkkönen et al., 2006). A route of formation involving T4 RNA ligase or T4 DNA ligase has also been proposed (Sillero et al., 2009). Though identification of the ApppI formation pathway was beyond the scope of this work, the high conservation of aminoacyl tRNA synthetases over evolutionary time (Perona and Hadd, 2012) makes this reaction plausible in both eukaryotes and prokaryotes such as *E. coli*. Suggestively, formation of ApppI by this mechanism consumes ATP in a futile cycle (**Figure 7D**). Depending on the concentrations of ApppI that build up and the kinetics of this back reaction, this futile cycle could contribute to the decreased ATP pool observed in strain 3Amk. Unfortunately, due to the difficulty in obtaining sufficient amounts of ApppI standard, only relative quantities of the ATP analog could be calculated. In future work, a more accurate estimation of intracellular concentrations of ApppI, coupled with *in vitro* work to assess the kinetics of the back reaction, may give clearer insight into whether this futile cycle plays a role in the observed toxicity.

Nucleotide analogs are frequently used as treatments for cancer and viral diseases due to their bioactivity and inhibitory effect on enzymes such as DNA polymerase, ribonucleotide reductase, and pyrimidine nucleoside phosphorylase (Jordheim et al., 2013). Nucleotide analogs

may also be incorporated into DNA, leading to DNA damage and the inhibition of cellular division or viral replication. Though research on the physiological consequences of ApppI accumulation is still limited, preliminary evidence points to considerable bioactivity: ApppI has been shown to inhibit the Adenosine Nucleotide Transporter (ANT) (Mönkkönen et al., 2006) and ATP-gated P23X receptor (Ishchenko et al., 2017) in eukaryotes. Inhibition of ANT has been directly linked to cell death and apoptosis in osteoclasts (Mönkkönen et al., 2006). ApppI can also bind to the surface of F1-ATPase (Mookerjee-Basu et al., 2010), an enzyme that is frequently inhibited by nucleotide analogs (Hong and Pedersen, 2008). Additional research is clearly necessary to determine the impact of ApppI accumulation on prokaryotic systems. Still, it is suggestive that genes involved in nucleotide metabolism and DNA damage repair were significantly upregulated in strain 3Amk at the same time ATP levels were reduced. These observations are consistent with known effects of certain nucleotide analogs and the potential inhibition of ATPase by ApppI, which would compound the effects of the futile cycle resulting from its formation (**Figure 7D**).

While the detection of ApppI in this study is exciting, we were unable to probe its toxicity directly due to the difficulty of synthesizing sufficient quantities of the analog. However, if the formation of ApppI is indeed the mediator of IPP associated toxicity in *E. coli*, engineering the host to overcome this stress may prove challenging. For example, if the back reaction from IPP and AMP-amino acid can be catalyzed by all aminoacyl tRNA synthetases, it would be a daunting task to engineer each enzyme to not promote the back reaction. If, however, only a subset of aminoacyl tRNA synthetases catalyze this back reaction, the engineering problem will prove much more tractable. Future *in vitro* studies that characterize each individual

aminoacyl tRNA synthetase's propensity to catalyze the formation of ApppI will hopefully guide rational engineering efforts to make more IPP tolerant hosts.

5. Conclusion

In this work, we design a three-strain experimental platform to isolate the impact of IPP toxicity from the stress associated with heterologous pathway expression. Using this platform, we assess the physiological consequences of IPP accumulation with complementary multi-omics data. We show that IPP accumulation is linked to reduced cell viability, pathway "breakage" at PMK, reduced nutrient uptake and ATP levels, and perturbed nucleotide metabolism. We also observe the extracellular accumulation of IPP and other phosphorylated intermediates, findings that could be relevant to the study of isoprenoid pathway "cross-talk" in other organisms. Finally, we show that IPP accumulation results in the formation of ApppI, a nucleotide analog of IPP known to be toxic to eukaryotes. Though additional work is needed, we propose that the formation of this metabolite may contribute to the observed IPP toxicity phenotypes. These data identify potential engineering targets for the alleviation of IPP toxicity and thus facilitate the construction of high-flux isoprenoid-producing strains.

Author Contributions

Conceptualization, K.W.G., M.G.T, and T.S.L.; Methodology, K.W.G., M.G.T., J.K., E.E.K.B., and C.J.P.; Investigation, K.W.G., M.G.T., J.K., E.E.K.B., G.W., V.T.B., L.J.G.C., V.B., and S.Y.; Writing – Original Draft, K.W.G., M.G.T., J.K, J.D.K., and T.S.L.; Writing – Review & Editing, K.W.G., M.G.T., J.K., J.D.K., and T.S.L.; Resources, T.S.L., J.D.K., C.J.P., P.D.A., and P.T.; Supervision, T.S.L. and J.D.K.; Funding Acquisition, T.S.L. and J.D.K.

Acknowledgments

This work was part of the DOE Joint BioEnergy Institute (http://www.jbei.org) supported by the US Department of Energy, Office of Science, Office of Biological and Environmental Research, through contract DE-AC02-05CH11231 between Lawrence Berkeley National Laboratory and the US Department of Energy. The United States Government retains and the publisher, by accepting the article for publication, acknowledges that the United States Government retains a non-exclusive, paid-up, irrevocable, world-wide license to publish or reproduce the published form of this manuscript, or allow others to do so, for United States Government purposes. This work used the Vincent J. Coates Genomics Sequencing Laboratory at UC Berkeley, supported by NIH S10 Instrumentation Grants S10RR029668 and S10RR027303.

Financial Interest

Jay Keasling has a financial interest in Amyris, Lygos, Demetrix, Constructive Biology and Napigen.

References

Atsumi, S., Wu, T.-Y., Machado, I.M.P., Huang, W.-C., Chen, P.-Y., Pellegrini, M., Liao, J.C., 2010. Evolution, genomic analysis, and reconstruction of isobutanol tolerance in *Escherichia coli*. Mol. Syst. Biol. doi:10.1038/msb.2010.98

Boyle, P.M., Silver, P.A., 2012. Parts plus pipes: Synthetic biology approaches to metabolic engineering. Metab. Eng. 14, 223–232. doi:DOI 10.1016/j.ymben.2011.10.003

Brunk, E., George, K.W., Alonso-Gutierrez, J., Thompson, M., Baidoo, E., Wang, G., Petzold,

C.J., McCloskey, D., Monk, J., Yang, L., O'Brien, E.J., Batth, T.S., Martin, H.G., Feist, A., Adams, P.D., Keasling, J.D., Palsson, B.O., Lee, T.S., 2016. Characterizing strain variation in engineered *E. coli* using a multi-omics-based workflow. Cell Syst. doi:10.1016/j.cels.2016.04.004

Brynildsen, M.P., Liao, J.C., 2009. An integrated network approach identifies the isobutanol response network of *Escherichia coli*. Mol. Syst. Biol. doi:10.1038/msb.2009.34

Castella, B., Kopecka, J., Sciancalepore, P., Mandili, G., Foglietta, M., Mitro, N., Caruso, D., Novelli, F., Riganti, C., Massaia, M., 2017. The ATP-binding cassette transporter A1 regulates phosphoantigen release and Vγ9Vδ2 T cell activation by dendritic cells. Nat. Commun. 8, 15663. doi:10.1038/ncomms15663

Chou, H.H., Keasling, J.D., 2013. Programming adaptive control to evolve increased metabolite production. Nat. Commun. 4. doi:10.1038/ncomms3595

Chubukov, V., Mingardon, F., Schackwitz, W., Baidoo, E.E.K., Alonso-Gutierrez, J., Hu, Q., Lee, T.S., Keasling, J.D., Mukhopadhyay, A., 2015. Acute limonene toxicity in *Escherichia coli* is caused by limonene hydroperoxide and alleviated by a point mutation in alkyl hydroperoxidase AhpC. Appl. Environ. Microbiol. doi:10.1128/AEM.01102-15

Chubukov, V., Mukhopadhyay, A., Petzold, C.J., Keasling, J.D., Martín, H.G., 2016. Synthetic and systems biology for microbial production of commodity chemicals. npj Syst. Biol. Appl. doi:10.1038/npjsba.2016.9

Foo, J.L., Jensen, H.M., Dahl, R.H., George, K., Keasling, J.D., Lee, T.S., Leong, S., Mukhopadhyay, A., 2014. Improving microbial biogasoline production in *Escherichia coli* using tolerance engineering, mBio, 5, e01932. doi: 10.1128/mBio.01932-14

George, K.W., Alonso-Gutierrez, J., Keasling, J.D., Lee, T.S., 2015a. Isoprenoid drugs, biofuels,

and chemicals - artemisinin, farnesene, and beyond. Adv. Biochem. Eng. Biotechnol. doi:10.1007/10_2014_288

George, K.W., Chen, A., Jain, A., Batth, T.S., Baidoo, E.E.K., Wang, G., Adams, P.D., Petzold, C.J., Keasling, J.D., Lee, T.S., 2014. Correlation analysis of targeted proteins and metabolites to assess and engineer microbial isopentenol production. Biotechnol. Bioeng. 111, 1648–1658. doi:10.1002/bit.25226

George, K.W., Thompson, M.G., Kang, A., Baidoo, E., Wang, G., Chan, L.J.G., Adams, P.D., Petzold, C.J., Keasling, J.D., Soon Lee, T., 2015b. Metabolic engineering for the high-yield production of isoprenoid-based C5 alcohols in *E. coli*. Sci. Rep. doi:10.1038/srep11128

González Fernández-Niño, S.M., Smith-Moritz, A.M., Chan, L.J.G., Adams, P.D., Heazlewood, J.L., Petzold, C.J., 2015. Standard flow liquid chromatography for shotgun proteomics in bioenergy research. Front. Bioeng. Biotechnol. 3, 44. doi:10.3389/fbioe.2015.00044

Hong, S., Pedersen, P.L., 2008. ATP synthase and the actions of inhibitors utilized to study its roles in human health, disease, and other scientific areas. Microbiol. Mol. Biol. Rev. doi:10.1128/MMBR.00016-08

Ishchenko, Y., Shakirzyanova, A., Giniatullina, R., Skorinkin, A., Bart, G., Turhanen, P., Määttä, J.A., Mönkkönen, J., Giniatullin, R., 2017. Selective calcium-dependent inhibition of ATP-gated P2X3 receptors by bisphosphonate-induced endogenous ATP analog ApppI. J. Pharmacol. Exp. Ther. J Pharmacol Exp Ther 361, 472–481. doi:10.1124/jpet.116.238840

Jones, J.A., Toparlak, T.D., Koffas, M.A.G., 2015. Metabolic pathway balancing and its role in the production of biofuels and chemicals. Curr. Opin. Biotechnol. doi:10.1016/j.copbio.2014.11.013

Jordheim, L.P., Durantel, D., Zoulim, F., Dumontet, C., 2013. Advances in the development of

nucleoside and nucleotide analogues for cancer and viral diseases. Nat. Rev. Drug Discov. 12, 447–464. doi:10.1038/nrd4010

Jullesson, D., David, F., Pfleger, B., Nielsen, J., 2015. Impact of synthetic biology and metabolic engineering on industrial production of fine chemicals. Biotechnol. Adv. doi:10.1016/j.biotechadv.2015.02.011

Kang, A., George, K.W., Wang, G., Baidoo, E., Keasling, J.D., Lee, T.S., 2016. Isopentenyl diphosphate (IPP)-bypass mevalonate pathways for isopentenol production. Metab. Eng. doi:10.1016/j.ymben.2015.12.002

Keasling, J.D., 2012. Synthetic biology and the development of tools for metabolic engineering. Metab. Eng. 14, 189–195. doi:DOI 10.1016/j.ymben.2012.01.004

Kizer, L., Pitera, D.J., Pfleger, B.F., Keasling, J.D., 2008. Application of functional genomics to pathway optimization for increased isoprenoid production. Appl. Environ. Microbiol. 74, 3229–41. doi:10.1128/AEM.02750-07

Li, H., Durbin, R., 2009. Fast and accurate short read alignment with Burrows-Wheeler transform. Bioinformatics 25, 1754–1760. doi:10.1093/bioinformatics/btp324

Liao, Y., Smyth, G.K., Shi, W., 2014. FeatureCounts: An efficient general purpose program for assigning sequence reads to genomic features. Bioinformatics 30, 923–930. doi:10.1093/bioinformatics/btt656

Ling, H., Teo, W., Chen, B., Leong, S.S.J., Chang, M.W., 2014. Microbial tolerance engineering toward biochemical production: From lignocellulose to products. Curr. Opin. Biotechnol. doi:10.1016/j.copbio.2014.03.005

Lipko, A., Swiezewska, E., 2016. Isoprenoid generating systems in plants - A handy toolbox how to assess contribution of the mevalonate and methylerythritol phosphate pathways to

the biosynthetic process. Prog. Lipid Res. 63, 70–92. doi:10.1016/j.plipres.2016.04.002

Love, M.I., Huber, W., Anders, S., Lönnstedt, I., Speed, T., Robinson, M., Smyth, G., McCarthy, D., Chen, Y., Smyth, G., Anders, S., Huber, W., Zhou, Y.-H., Xia, K., Wright, F., Wu, H., Wang, C., Wu, Z., Hardcastle, T., Kelly, K., Wiel, M. Van De, Leday, G., Pardo, L., Rue, H., Vaart, A. Van Der, Wieringen, W. Van, Boer, J., Huber, W., Sültmann, H., Wilmer, F., Heydebreck, A. von, Haas, S., Korn, B., Gunawan, B., Vente, A., Füzesi, L., Vingron, M., Poustka, A., Gentleman, R., Carey, V., Bates, D., Bolstad, B., Dettling, M., Dudoit, S., Ellis, B., Gautier, L., Ge, Y., Gentry, J., Hornik, K., Hothorn, T., Huber, W., Iacus, S., Irizarry, R., Leisch, F., Li, C., Maechler, M., Rossini, A., Sawitzki, G., Smith, C., Smyth, G., Tierney, L., Yang, J., Zhang, J., McCullagh, P., Nelder, J., Hansen, K., Irizarry, R., Wu, Z., Risso, D., Schwartz, K., Sherlock, G., Dudoit, S., Smyth, G., Bottomly, D., Walter, N., Hunter, J., Darakjian, P., Kawane, S., Buck, K., Searles, R., Mooney, M., McWeeney, S., Hitzemann, R., Pickrell, J., Marioni, J., Pai, A., Degner, J., Engelhardt, B., Nkadori, E., Veyrieras, J.-B., Stephens, M., Gilad, Y., Pritchard, J., Hastie, T., Tibshirani, R., Friedman, J., Bi, Y., Davuluri, R., Feng, J., Meyer, C., Wang, Q., Liu, J., Liu, X., Zhang, Y., Benjamini, Y., Hochberg, Y., Bourgon, R., Gentleman, R., Huber, W., McCarthy, D., Smyth, G., Li, J., Tibshirani, R., Cook, R., Hammer, P., Banck, M., Amberg, R., Wang, C., Petznick, G., Luo, S., Khrebtukova, I., Schroth, G., Beyerlein, P., Beutler, A., Frazee, A., Langmead, B., Leek, J., Trapnell, C., Hendrickson, D., Sauvageau, M., Goff, L., Rinn, J., Pachter, L., Glaus, P., Honkela, A., Rattray, M., Anders, S., Reyes, A., Huber, W., Sammeth, M., Robinson, M., McCarthy, D., Smyth, G., Zhou, X., Lindsay, H., Robinson, M., Leng, N., Dawson, J., Thomson, J., Ruotti, V., Rissman, A., Smits, B., Haag, J., Gould, M., Stewart, R., Kendziorski, C., Law, C., Chen, Y., Shi, W., Smyth, G., Hubert, L., Arabie,

P., Witten, D., Irizarry, R., Wu, Z., Jaffee, H., Asangani, I., Dommeti, V., Wang, X., Malik, R., Cieslik, M., Yang, R., Escara-Wilke, J., Wilder-Romans, K., Dhanireddy, S., Engelke, C., Iyer, M., Jing, X., Wu, Y.-M., Cao, X., Qin, Z., Wang, S., Feng, F., Chinnaiyan, A., Ross-Innes, C., Stark, R., Teschendorff, A., Holmes, K., Ali, H., Dunning, M., Brown, G., Gojis, O., Ellis, I., Green, A., Ali, S., Chin, S.-F., Palmieri, C., Caldas, C., Carroll, J., Robinson, D., Chen, W., Storey, J., Gresham, D., McMurdie, P., Holmes, S., Vasquez, J., Hon, C., Vanselow, J., Schlosser, A., Siegel, T., Zhou, Y., Zhu, S., Cai, C., Yuan, P., Li, C., Huang, Y., Wei, W., Cox, D., Reid, N., Robinson, M., Smyth, G., Pawitan, Y., Armijo, L., Di, Y., Schafer, D., Cumbie, J., Chang, J., Abramowitz, M., Stegun, I., Newton, M., Kendziorski, C., Richmond, C., Blattner, F., Tsui, K., Huber, W., Heydebreck, A. von, Sultmann, H., Poustka, A., Vingron, M., Durbin, B., Hardin, J., Hawkins, D., Rocke, D., Friedman, J., Hastie, T., Tibshirani, R., Cule, E., Vineis, P., Iorio, M. De, Cook, R., Weisberg, S., Lawrence, M., Huber, W., Pagès, H., Aboyoun, P., Carlson, M., Gentleman, R., Morgan, M., Carey, V., Anders, S., Pyl, P., Huber, W., Delhomme, N., Padioleau, I., Furlong, E., Steinmetz, L., Liao, Y., Smyth, G., Shi, W., Kim, D., Pertea, G., Trapnell, C., Pimentel, H., Kelley, R., Salzberg, S., 2014. Moderated estimation of fold change and dispersion for RNA-seq data with DESeq2. Genome Biol. 15, 550. doi:10.1186/s13059-014-0550-8

Martin, V.J., Pitera, D.J., Withers, S.T., Newman, J.D., Keasling, J.D., 2003. Engineering a mevalonate pathway in *Escherichia coli* for production of terpenoids. Nat Biotechnol 21, 796–802. doi:10.1038/nbt833nbt833 [pii]

Mönkkönen, H., Auriola, S., Lehenkari, P., Kellinsalmi, M., Hassinen, I.E., Vepsäläinen, J., Mönkkönen, J., 2006. A new endogenous ATP analog (ApppI) inhibits the mitochondrial

adenine nucleotide translocase (ANT) and is responsible for the apoptosis induced by nitrogen-containing bisphosphonates. Br. J. Pharmacol. doi:10.1038/sj.bjp.0706628

Mookerjee-Basu, J., Vantourout, P., Martinez, L.O., Perret, B., Collet, X., Perigaud, C., Peyrottes, S., Champagne, E., 2010. F1-adenosine triphosphatase displays properties characteristic of an antigen presentation molecule for V 9V 2 T cells. J. Immunol. doi:10.4049/jimmunol.0904024

Mukhopadhyay, A., 2015. Tolerance engineering in bacteria for the production of advanced biofuels and chemicals. Trends Microbiol. doi:10.1016/j.tim.2015.04.008

Nicolaou, S.A., Gaida, S.M., Papoutsakis, E.T., 2010. A comparative view of metabolite and substrate stress and tolerance in microbial bioprocessing: From biofuels and chemicals, to biocatalysis and bioremediation. Metab. Eng. doi:10.1016/j.ymben.2010.03.004

Paddon, C.J., Keasling, J.D., 2014. Semi-synthetic artemisinin: a model for the use of synthetic biology in pharmaceutical development. Nat. Rev. Microbiol. 12, 355–67. doi:10.1038/nrmicro3240

Perona, J.J., Hadd, A., 2012. Structural diversity and protein engineering of the aminoacyl-tRNA synthetases. Biochemistry. doi:10.1021/bi301180x

Shannon, P.T., Grimes, M., Kutlu, B., Bot, J.J., Galas, D.J., 2013. RCytoscape: tools for exploratory network analysis. BMC Bioinformatics 14, 217. doi:10.1186/1471-2105-14-217

Sillero, M.A.G., de Diego, A., Tavares, J.E.F., Silva, J.A.D.C. da, Pérez-Zúñiga, F.J., Sillero, A., 2009. Synthesis of ATP derivatives of compounds of the mevalonate pathway (isopentenyl di- and triphosphate; geranyl di- and triphosphate, farnesyl di- and triphosphate, and dimethylallyl diphosphate) catalyzed by T4 RNA ligase, T4 DNA ligase and other ligases. Potential relationship with the effect of bisphosphonates on osteoclasts. Biochem.

Pharmacol. 78, 335–343. doi:10.1016/j.bcp.2009.04.028

Sun, P., Schuurink, R.C., Caissard, J.C., Hugueney, P., Baudino, S., 2016. My Way: Noncanonical biosynthesis pathways for plant volatiles. Trends Plant Sci. 21, 884–894. doi:10.1016/j.tplants.2016.07.007

Weisell, J., Vepsäläinen, J., Turhanen, P.A., 2015. Two strategies for the synthesis of the biologically important ATP analogue APPPI, at a multi-milligram scale. Beilstein J. Org. Chem. doi:10.3762/bjoc.11.237

Wu, G., Yan, Q., Jones, J.A., Tang, Y.J., Fong, S.S., Koffas, M.A.G., 2016. Metabolic burden: cornerstones in synthetic biology and metabolic engineering applications. Trends Biotechnol. 34, 652-664. doi:10.1016/j.tibtech.2016.02.010

Yu, G., Wang, L.-G., Han, Y., He, Q.-Y., 2012. clusterProfiler: an R package for comparing biological themes among gene clusters. OMICS 16, 284–7. doi:10.1089/omi.2011.0118

Zheng, Y., Liu, Q., Li, L., Qin, W., Yang, J., Zhang, H., Jiang, X., Cheng, T., Liu, W., Xu, X., Xian, M., 2013. Metabolic engineering of *Escherichia coli* for high-specificity production of isoprenol and prenol as next generation of biofuels. Biotechnol. Biofuels. doi:10.1186/1754-6834-6-57

Zhou, K., Zou, R., Stephanopoulos, G., Too, H.P., 2012. Metabolite profiling identified methylerythritol cyclodiphosphate efflux as a limiting step in microbial isoprenoid production. PLoS One 7. doi:10.1371/journal.pone.0047513

Figure legends

Figure 1. Experimental platform to study IPP toxicity. (A) Isoprenol pathway reactions and associated heterologous genes. 7 genes were overexpressed in a plasmid-based isoprenol biosynthetic pathway. The conversion of IP to isoprenol proceeds via native *E. coli* phosphatases. In the current pathway, HMGS and HMGR are derived from *Staphylococcus aureus* (*mvaS* and *mvaA*, respectively), MK, PMK, and PMD are derived from *Saccharomyces cerevisiae*, and AtoB and NudB are derived from *E. coli*. (B) Plasmid architecture in strain 3A, 3Amk, and DH1-EV (WT). Each strain harbored 2 plasmids. For strains 3A and 3Amk, plasmid 1 (medium copy p15A ori) contained a single operon of the first 5 genes of the pathway driven by a lacUV5 promoter. Plasmid 2 (high copy ColE1 ori) contained *nudB* and PMD driven by a Trc promoter. In strain 3Amk, an additional copy of MK was placed on plasmid 2. Strain DH1-EV (WT) contained versions of plasmid 1 and plasmid 2 that contained no promoter and no heterologous pathway genes. (C) IPP, OD, and isoprenol levels in each strain. The x-axis shows time post-induction in hours, referred to in subsequent figures as "hours" for the purpose of simplification. Note that a log scale is used for OD_{600nm}. Error bars represent standard deviation of the mean (n = 3). Note that error bars are obscured by the markers in most cases.

Figure 2. Physiological impact of IPP accumulation. (A) Incidence of dead cells in strains 3A and 3Amk. % dead cells in cultures of strains 3A and 3Amk were quantified using live/dead staining coupled with FACs. Error bars represent standard deviation of the mean (n = 3). (B) Strain 3Amk live/dead micrograph. Representative micrograph of strain 3Amk at 6 hours post-

induction following live/dead staining. Note the presence of elongated cells and a staining phenotype consistent with compromised membrane integrity. (C) Strain 3A live/dead micrograph. Representative micrograph of strain 3A at 6 hours post-induction following live/dead staining. (D) Comparison of CFUs vs. OD for strain 3A and 3Amk. CFUs were recovered on LB agar for comparison with $OD_{600\ nm}$ (dashed lines). Note the striking decrease in CFUs from 0 to 6 hours post-induction for strain 3Amk, which occurred despite a >2-fold increase in OD. Error bars show standard deviation of the mean (n = 3). (E) CFUs on selective and non-selective media for strain 3Amk. By 24 hours, there were fewer CFUs recovered on selective media ("Cm" = chloramphenicol, "Cb" = carbenicillin) than on non-selective media ("LB"). The number of asterisks (*) denote varying levels of significance (see legend for relative p-values). Error bars show standard deviation of the mean (n = 3). (F) CFUs on selective and non-selective media for strain 3A. The number of asterisks (*) denote varying levels of significance (see legend for relative p-values). Error bars represent standard deviation of the mean (n = 3).

Figure 3. PMK protein expression is attenuated in strain 3Amk in response to IPP accumulation. (A) Pathway proteomics. Shotgun proteomics samples were collected over an 18-hour time course to assess protein expression and stability. Concentrations are presented in relative units (R.U.). PMK protein levels (*) are highlighted to show decrease at 6 hours. Error bars represent standard deviation of the mean (n = 3). See also Figure S2. (B) Pathway metabolomics. Intracellular concentrations of each metabolite are shown in mM, extracellular isoprenol concentrations are in mg/L. Mev-PP levels (*) are highlighted to show decrease at 6 hours. Error bars represent standard deviation of the mean (n = 3). (C) IPP bypass explains continued

isoprenol production. Disruption of PMK (red "X") will still permit isoprenol production through an "IPP bypass" pathway catalyzed by PMD. Isoprenol concentrations in strain 3Amk are shown with an adjusted scale to highlight continued production despite a decrease in PMK levels.

Figure 4. Aggregate metabolomics data set and representative analyses. (A) Measured intracellular metabolites and relative concentrations over time. Mean intracellular concentrations (n = 3) of each metabolite are shown for each time point. Relative concentrations were determined by log2 transformation after adding a small constant. See Supplemental File S1, Jupyter R notebook "IPP_metabolomics" for more information. (B) Measured extracellular metabolites and relative concentrations over time. Mean extracellular concentrations (n = 3) of each metabolite are shown for each time point. (C) Plot of the first 4 principal components of the intracellular data. Principal components analysis was performed using log2 transformed data and the contributions of top four metabolites to the pair of principal components were shown as arrows. See Supplemental File S1, Jupyter R notebook "IPP_metabolomics" for more information. (D) Plot of the first 4 principal components of the extracellular data. (E) ATP concentration and energy charge is reduced in strain 3Amk. Error bars show standard deviation of the mean (n = 3). (F) Nutrient uptake is reduced during periods of IPP accumulation. Extracellular glucose concentrations (in mM) and extracellular valine concentrations (in µM) are shown. Error bars represent standard deviation of the mean (n = 3).

Figure 5. Evidence of IPP uptake in strain 3Amk. (A) Intracellular and extracellular IPP in strain 3Amk. Error bars represent standard deviation of the mean (n = 3). (B) Experimental design to

evaluate IPP stability. (C) IPP in supernatant collected at t = 6 hours. IPP is stable in filter sterilized (FS) and 3 kDa molecular weight cut-off (MWCO) treatments. Error bars show standard deviation of the mean (n = 3). (D) IPP in supernatant collected at t = 15 hours. IPP is again stable in both treatments. Error bars represent standard deviation of the mean (n = 3).

Figure 6. Shared and distinct transcriptomic responses in 3A and 3Amk. (A) Venn diagrams of significantly upregulated or downregulated genes (adjusted p-value < 0.1 and |log2 fold change| > 1) in strain 3A and 3Amk at 1 and 12 hours post-induction. (B) and (C) Functional enrichment of differentially expressed genes (adjusted p-value < 0.1) in 3A only, 3Amk only, or both 3A and 3Amk at t = 1 hour and 12 hours, respectively.

Figure 7. Accumulation of ATP analog ApppI in strain 3Amk. (A) Chemical structures of ApppI and IPP. (B) A compound consistent with ApppI (m/z 574) accumulates in strain 3Amk and is correlated with IPP accumulation. An anticorrelation with ATP levels is also observed. Error bars represent standard deviation of the mean (n = 3). *Putative ApppI concentrations in mM were calculated based on the standard curve of ATP since a reliable ApppI standard curve was not available for quantitation. (C) The putative ApppI peak in strain 3Amk is consistent with a chemically synthesized standard. Note that while a small peak is present in strain 3A, the compound is not present in WT. Chromatograms from 3 biological replicates are shown. (D) The formation of ApppI could result in a futile cycle that drains ATP levels. Preliminary evidence suggests that ApppI binds ATPase, which could further inhibit ATP production.

Supplemental Figures

Figure S1. Pathway induction is required for growth inhibition. Induced (filled shapes) cultures of strain 3Amk (0.5 mM IPTG added) show growth inhibition relative to uninduced (open shapes) controls, presumably due to IPP accumulation. Strain 3A grows similarly in each state. Error bars show standard deviation of the mean (n = 3).

Figure S2. Reduced levels of Beta-Lactamase and LacI in strain 3Amk suggest a reduction in plasmid copy number. Levels of PMD and NudB protein were reduced in strain 3Amk relative to strain 3A. Genes encoding both proteins were located on plasmid 2. LacI and β-Lactamase, 2 proteins encoded by genes present on the plasmid 2 vector backbone, are also reduced in strain 3Amk. These data suggest that a reduction in plasmid copy number was the most probable cause of reduced PMD and NudB protein levels in strain 3Amk. Error bars show standard deviation of the mean (n = 3).

Figure S3. Reinoculation of strain 3Amk reveals pathway breakage. (A) Cultures of 3A and 3Amk were induced with 0.5 mM IPTG, grown for 24 hours ("primary" cultures) and subsequently used as inoculum for fresh cultures that underwent a second round of growth and induction ("secondary" cultures). Primary and secondary cultures were monitored for growth at 0, 3, 6, and 20 hours post-induction and isoprenol production at 20 hours post-induction. Secondary cultures of strain 3Amk grew more rapidly than primary cultures while producing no detectable isoprenol. Error bars show standard deviation of the mean (n = 3). (B) The experiment was repeated with 3Amk only. IPP concentrations were measured at t = 6 hours post-induction (black triangles) in both the primary and secondary cultures. While IPP was high

in the growth-inhibited primary cultures, IPP was at wild-type levels in the secondary culture. Error bars show standard deviation of the mean (n = 3).

Figure S4. Proline and betaine, metabolites associated with osmotic stress, are elevated in strain 3Amk. Error bars represent standard deviation of the mean (n = 3).

Figure S5. MEP pathway intermediate MEcPP accumulates and appears to be exported by strain 3A. Data from strain 3A is shown. Error bars show standard deviation of the mean (n = 3).

Figure S6. IP is found outside the cell in 3A and 3Amk and is stable in culture media. (A) Extracellular IP in 3A and 3Amk. Error bars show standard deviation of the mean (n = 3). (B) IP is stable in the culture media. See Figure 5 for experimental set-up. All other pathway intermediates were also stable in culture media (data not shown). Error bars represent standard deviation of the mean.

Figure S7. MVA pathway transcript levels of strain 3A (A) and strain 3Amk (B) at 1 and 12 hours post-induction. Protein levels are shown for comparison. Transcript error bars show standard deviation of the mean (n = 2). Protein error bars show standard deviation of the mean (n = 3).

Figure 1

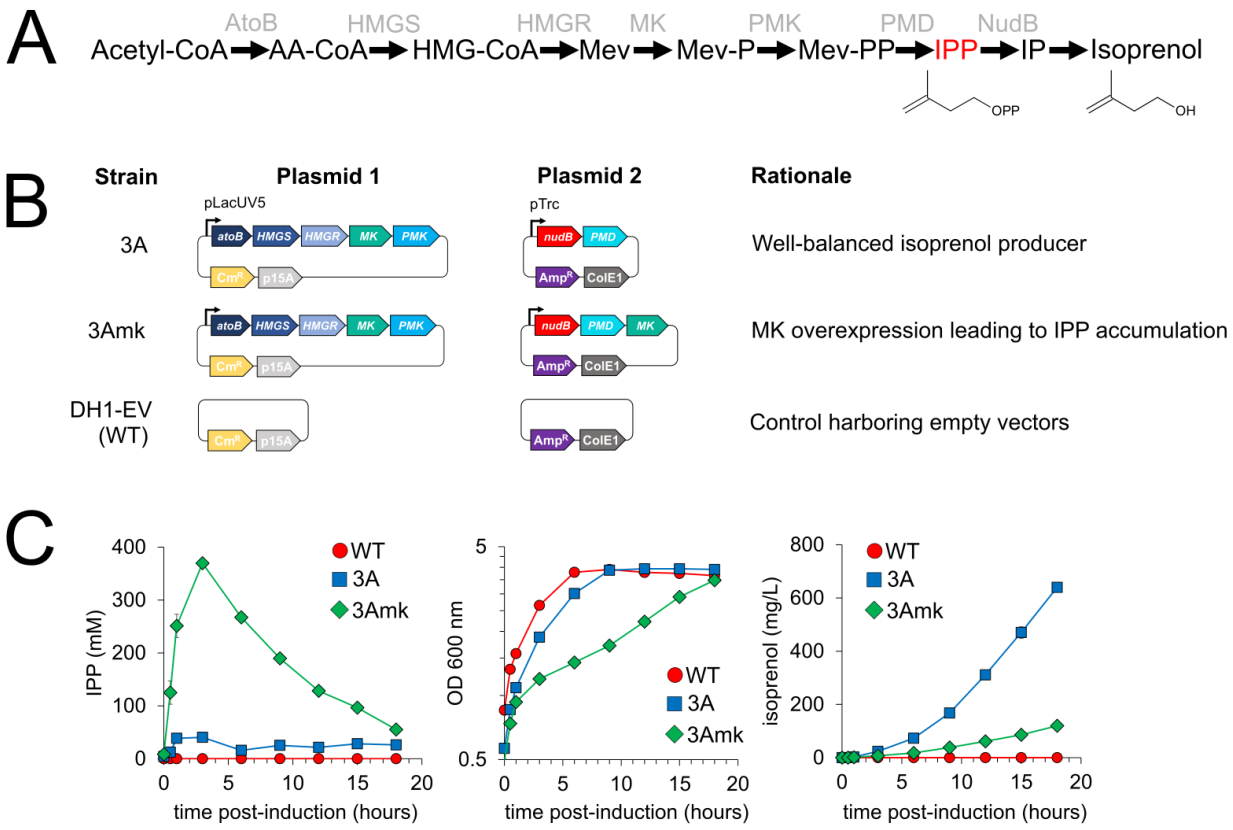
A
AtoB
HMGS
HMGR
MK
PMK
PMD
NudB
Acetyl-CoA
AA-CoA
HMG-CoA
Mev
Mev-P
Mev-PP
IPP
IP
Isoprenol
OPP
OH
B
Strain
Plasmid 1
Plasmid 2
Rationale
pLacUV5
pTrc
3A
Well-balanced isoprenol producer
3Amk
MK overexpression leading to IPP accumulation
DH1-EV (WT)
Control harboring empty vectors
atoB
HMGS
HMGR
MK
PMK
nudB
PMD
CmR
p15A
AmpR
ColE1
C
IPP (mM)
OD 600 nm
isoprenol (mg/L)
time post-induction (hours)
WT
3A
3Amk

Figure 2

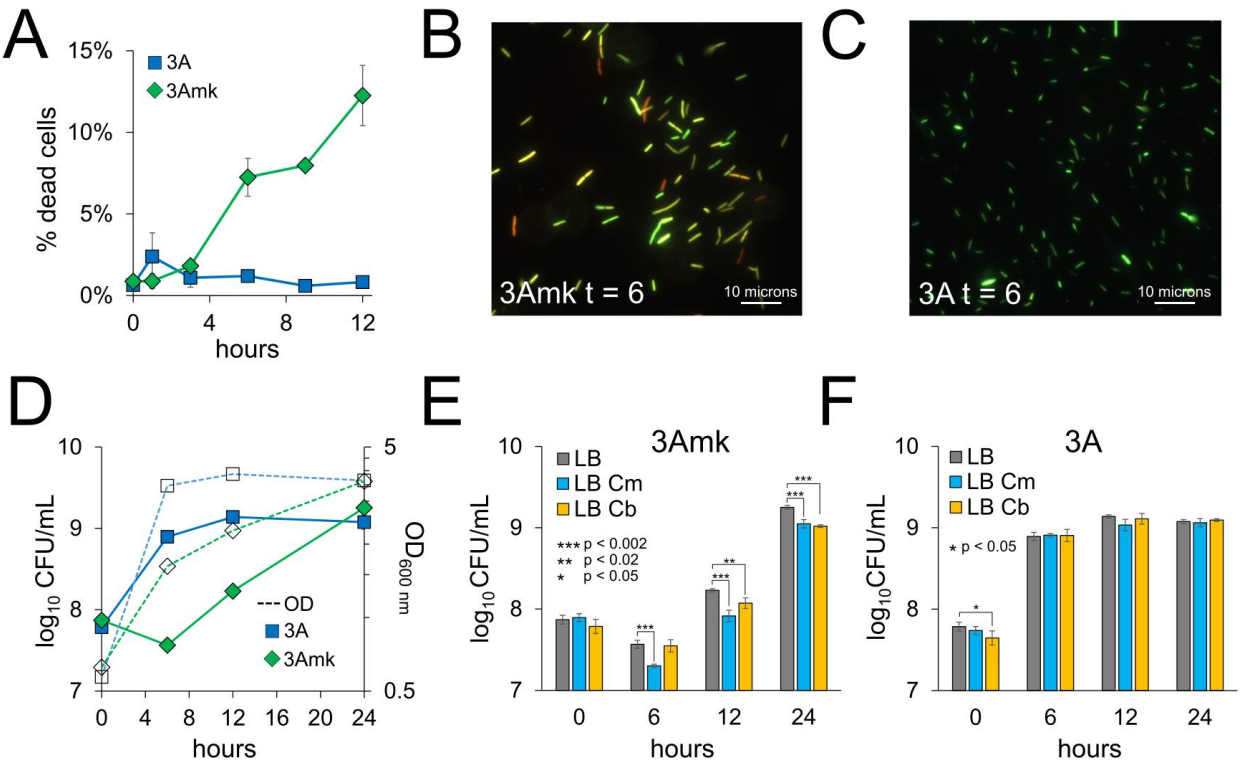
A
15%
10%
5%
0%
% dead cells
3A
3Amk
0
4
8
12
hours
B
3Amk t = 6
10 microns
C
3A t = 6
10 microns
D
10
9
8
7
log10 CFU/mL
5
0.5
OD600 nm
--- OD
3A
3Amk
0
4
8
12
16
20
24
hours
E
3Amk
LB
LB Cm
LB Cb
*** p < 0.002
** p < 0.02
* p < 0.05
log10 CFU/mL
0
6
12
24
hours
F
3A
LB
LB Cm
LB Cb
* p < 0.05
log10CFU/mL
0
6
12
24
hours

Figure 3

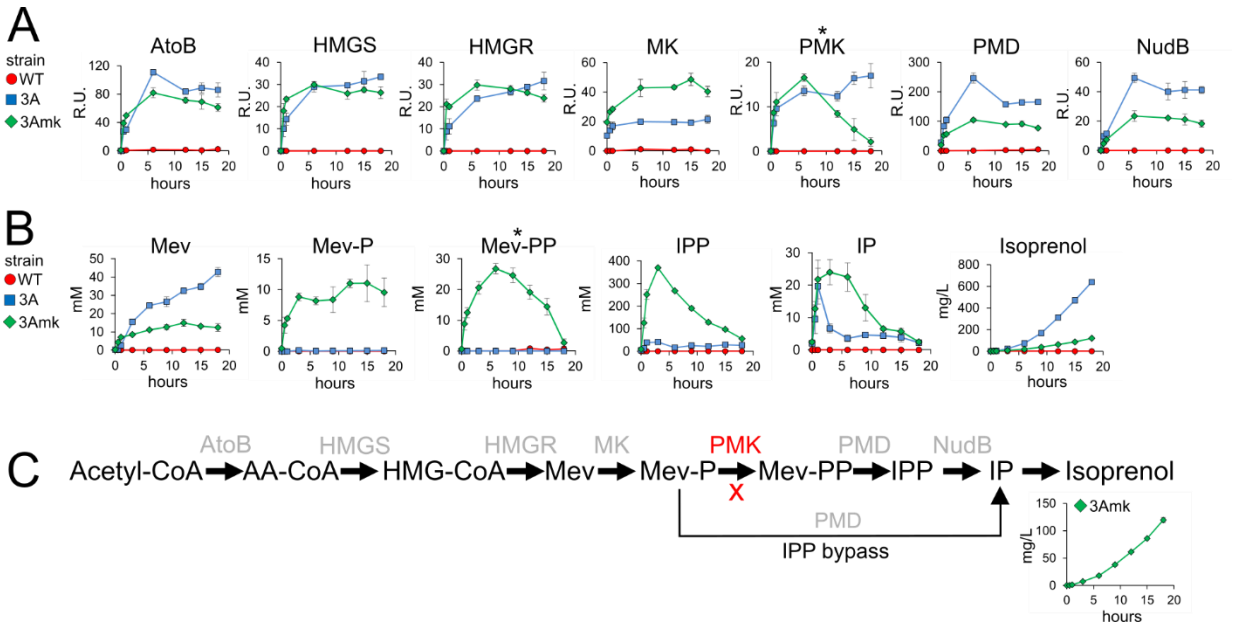
A
strain
WT
3A
3Amk
AtoB
HMGS
HMGR
MK
*PMK
PMD
NudB
R.U.
hours
B
Mev
Mev-P
*Mev-PP
IPP
IP
Isoprenol
mM
mg/L
C
AtoB
HMGS
HMGR
MK
PMK
PMD
NudB
Acetyl-CoA
AA-CoA
HMG-CoA
Mev
Mev-P
Mev-PP
IPP
IP
Isoprenol
X
PMD
IPP bypass
3Amk

Figure 4

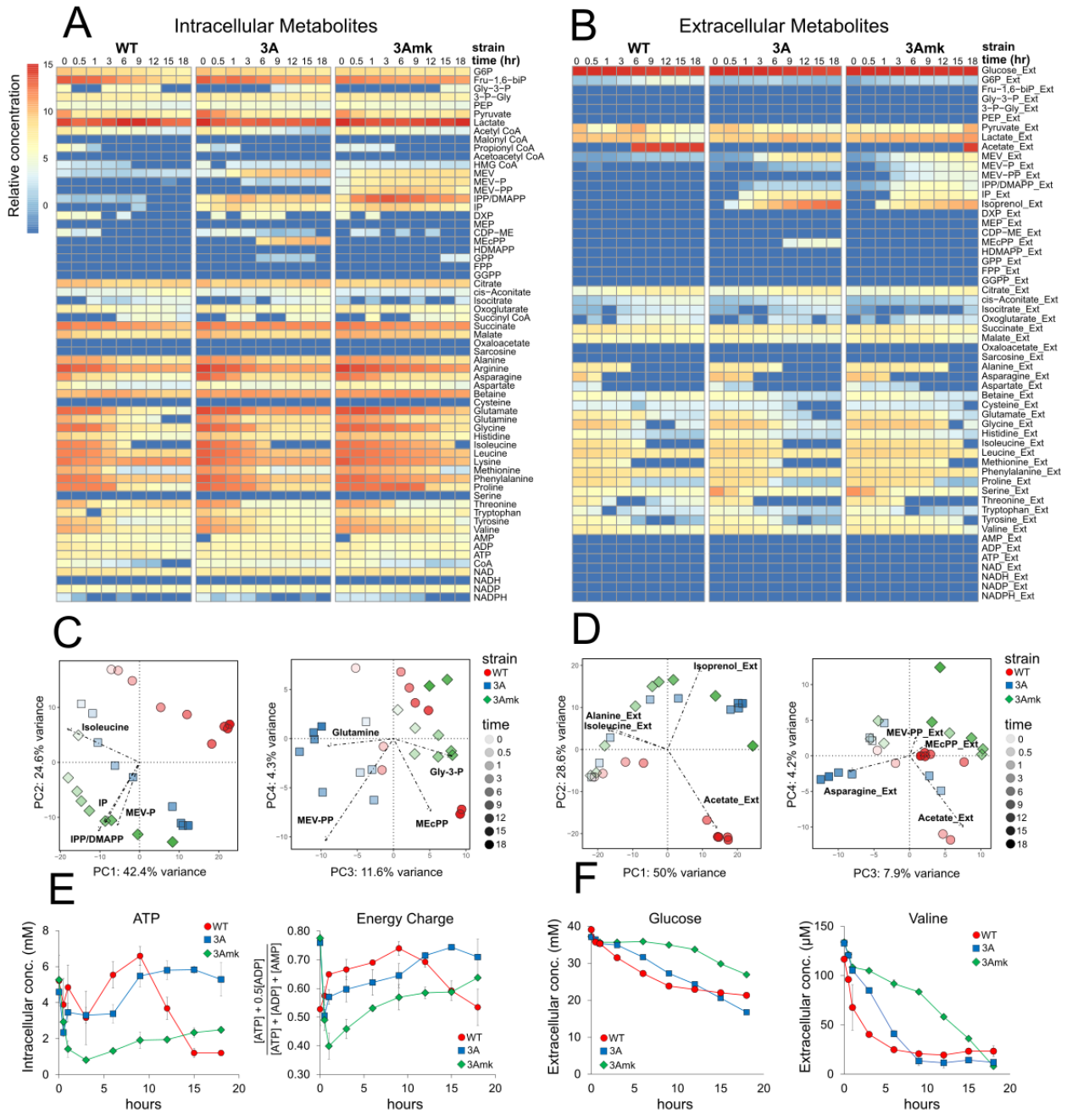
A
Intracellular Metabolites
WT
3A
3Amk
strain
time (hr)
Relative concentration
B
Extracellular Metabolites
C
PC2: 24.6% variance
PC1: 42.4% variance
PC4: 4.3% variance
PC3: 11.6% variance
Isoleucine
IP
MEV-P
IPP/DMAPP
Glutamine
Gly-3-P
MEV-PP
MEcPP
D
PC2: 28.6% variance
PC1: 50% variance
PC4: 4.2% variance
PC3: 7.9% variance
Isoprenol_Ext
Alanine_Ext
Isoleucine_Ext
Acetate_Ext
MEV-PP_Ext
MEcPP_Ext
Asparagine_Ext
Acetate_Ext
strain
WT
3A
3Amk
time
E
ATP
Intracellular conc. (mM)
hours
Energy Charge
[ATP] + 0.5[ADP] / [ATP] + [ADP] + [AMP]
F
Glucose
Extracellular conc. (mM)
Valine
Extracellular conc. (μM)

Figure 5

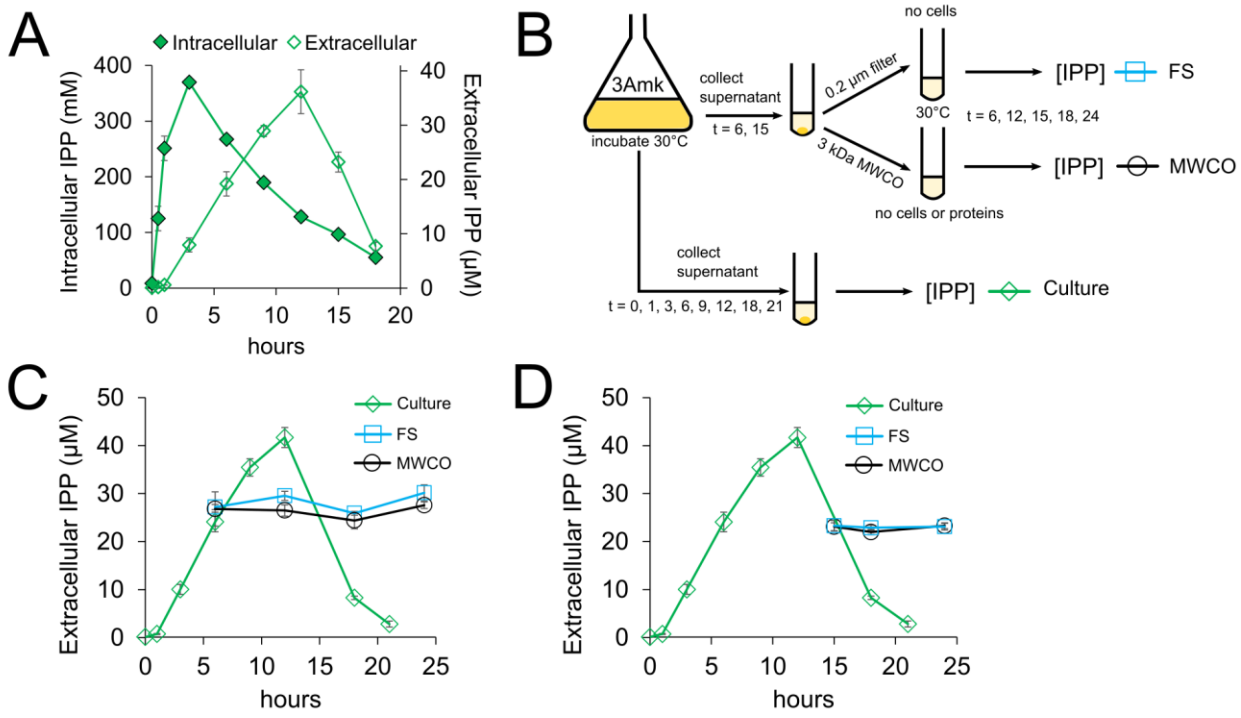
A
Intracellular
Extracellular
Intracellular IPP (mM)
Extracellular IPP (µM)
hours
B
3Amk
incubate 30°C
collect supernatant
t = 6, 15
0.2 µm filter
3 kDa MWCO
no cells
30°C
t = 6, 12, 15, 18, 24
no cells or proteins
[IPP]
FS
MWCO
collect supernatant
t = 0, 1, 3, 6, 9, 12, 18, 21
Culture
C
Culture
FS
MWCO
Extracellular IPP (µM)
hours
D
Culture
FS
MWCO
Extracellular IPP (µM)
hours

Figure 6

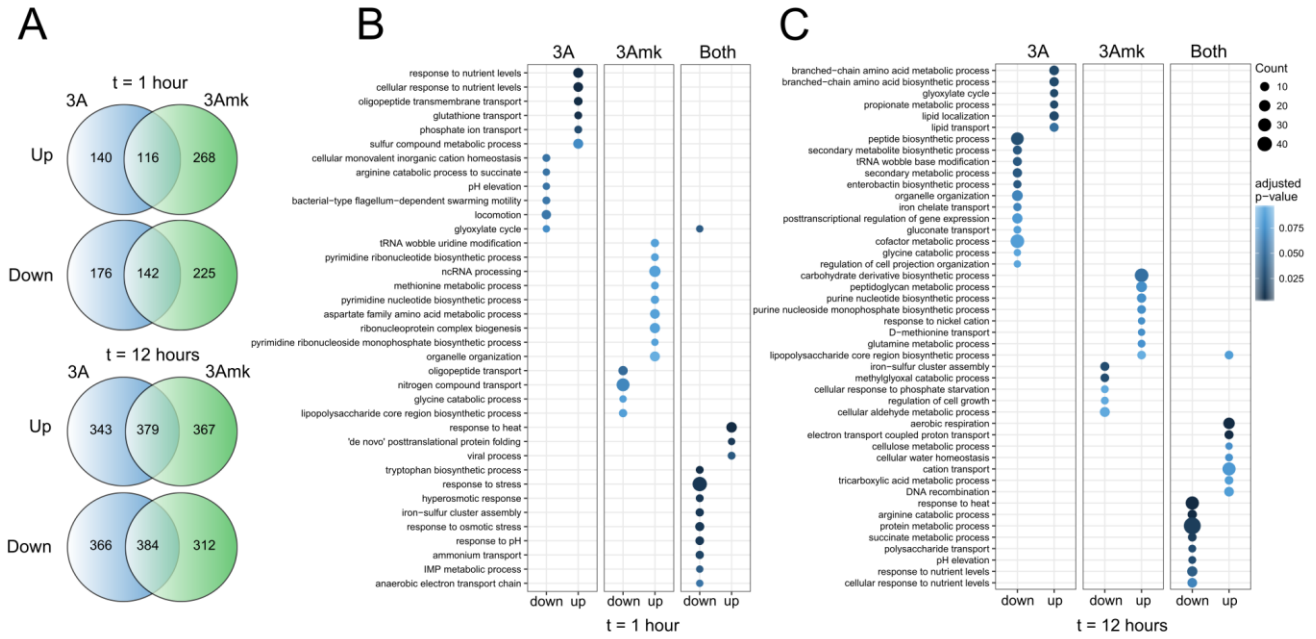
A
t = 1 hour
3A
3Amk
Up
140
116
268
Down
176
142
225
t = 12 hours
3A
3Amk
Up
343
379
367
Down
366
384
312
B
3A
3Amk
Both
response to nutrient levels
cellular response to nutrient levels
oligopeptide transmembrane transport
glutathione transport
phosphate ion transport
sulfur compound metabolic process
cellular monovalent inorganic cation homeostasis
arginine catabolic process to succinate
pH elevation
bacterial−type flagellum−dependent swarming motility
locomotion
glyoxylate cycle
tRNA wobble uridine modification
pyrimidine ribonucleotide biosynthetic process
ncRNA processing
methionine metabolic process
pyrimidine nucleotide biosynthetic process
aspartate family amino acid metabolic process
ribonucleoprotein complex biogenesis
pyrimidine ribonucleoside monophosphate biosynthetic process
organelle organization
oligopeptide transport
nitrogen compound transport
glycine catabolic process
lipopolysaccharide core region biosynthetic process
response to heat
'de novo' posttranslational protein folding
viral process
tryptophan biosynthetic process
response to stress
hyperosmotic response
iron−sulfur cluster assembly
response to osmotic stress
response to pH
ammonium transport
IMP metabolic process
anaerobic electron transport chain
down up down up down up
t = 1 hour
C
3A
3Amk
Both
branched−chain amino acid metabolic process
branched−chain amino acid biosynthetic process
glyoxylate cycle
propionate metabolic process
lipid localization
lipid transport
peptide biosynthetic process
secondary metabolite biosynthetic process
tRNA wobble base modification
secondary metabolic process
enterobactin biosynthetic process
organelle organization
iron chelate transport
posttranscriptional regulation of gene expression
gluconate transport
cofactor metabolic process
glycine catabolic process
regulation of cell projection organization
carbohydrate derivative biosynthetic process
peptidoglycan metabolic process
purine nucleotide biosynthetic process
purine nucleoside monophosphate biosynthetic process
response to nickel cation
D−methionine transport
glutamine metabolic process
lipopolysaccharide core region biosynthetic process
iron−sulfur cluster assembly
methylglyoxal catabolic process
cellular response to phosphate starvation
regulation of cell growth
cellular aldehyde metabolic process
aerobic respiration
electron transport coupled proton transport
cellulose metabolic process
cellular water homeostasis
cation transport
tricarboxylic acid metabolic process
DNA recombination
response to heat
arginine catabolic process
protein metabolic process
succinate metabolic process
polysaccharide transport
pH elevation
response to nutrient levels
cellular response to nutrient levels
down up down up down up
t = 12 hours
Count
10
20
30
40
adjusted p−value
0.075
0.050
0.025

Figure 7

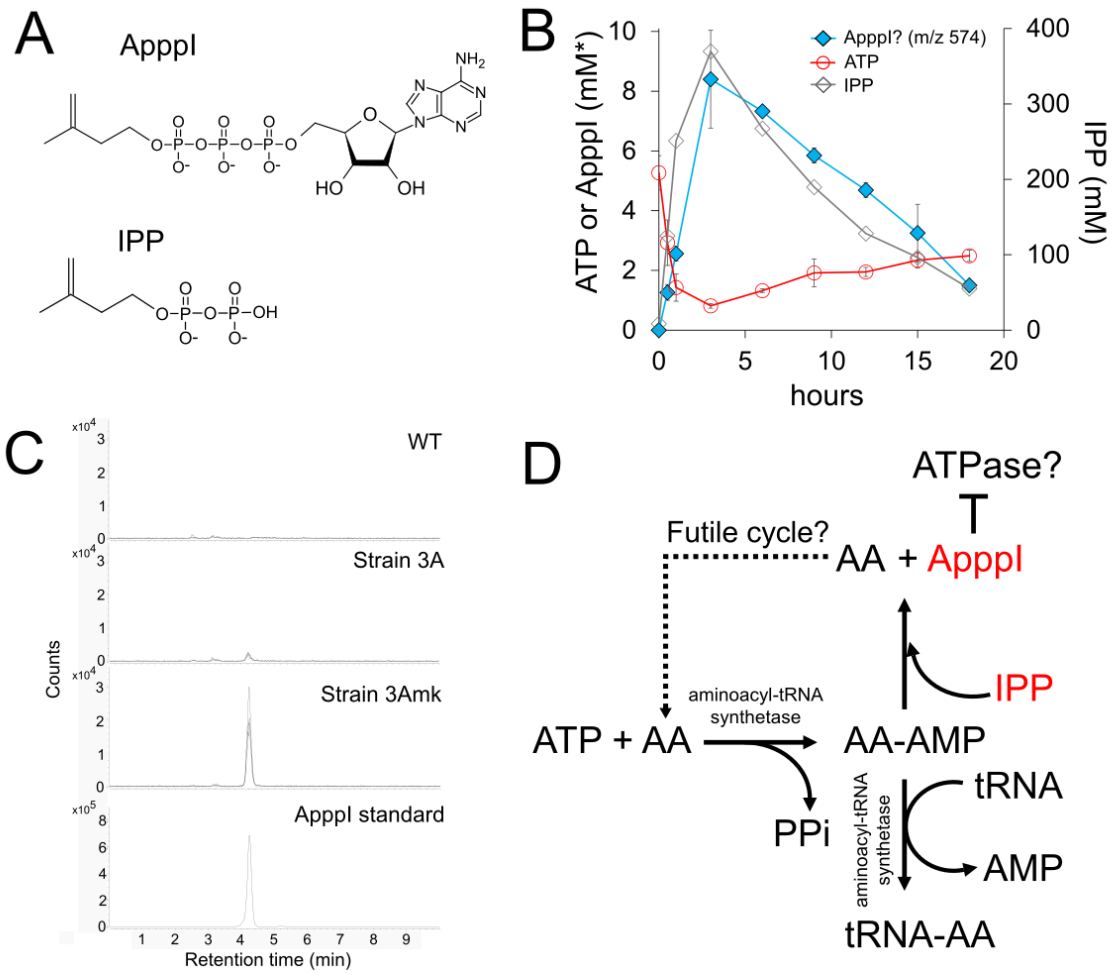
A
ApppI
IPP
B
ApppI? (m/z 574)
ATP
IPP
ATP or ApppI (mM*)
IPP (mM)
hours
C
WT
Strain 3A
Strain 3Amk
ApppI standard
Counts
Retention time (min)
D
ATPase?
Futile cycle?
AA + ApppI
IPP
aminoacyl-tRNA synthetase
ATP + AA
AA-AMP
PPi
tRNA
AMP
tRNA-AA